Manuscript_revision accepted

manuscript submitted to *QR* *Monday, May 23, 2022*

High-resolution magnetochronology detects multiple stages of Pleistocene tectonic uplift and deformation in the Po Plain of northern Italy

Serena Perini[1]*, Giovanni Muttoni[1], Franz Livio[2], Michele Zucali[1], Alessandro M. Michetti[2,3] and Andrea Zerboni[1]

[1] Dipartimento di Scienze della Terra 'Ardito Desio', Università degli Studi di Milano, via Luigi Mangiagalli 34, 20133 Milano, Italia

[2] Dipartimento di Scienza e Alta Tecnologia, Università degli Studi dell'Insubria, via Valleggio 11, 22100, Como, Italia

[3] INGV, Istituto Nazionale di Geofisica e Vulcanologia, Sezione di Napoli Osservatorio Vesuviano, Via Diocleziano, 328, 80124 Napoli, Italia

*Corresponding author: Serena Perini (serena.perini@unimi.it)

Abstract

We developed a high-resolution magnetochronology of the Pleistocene stratigraphy of the Monte Netto hillock, a tectonically uplifted structure in the Po Plain of northern Italy. Our data allowed reconstructing the depositional age of the sequence and assessing rates of deformation and rock uplift of the neotectonic structure, thus providing constraints on the tectono-sedimentary evolution of this seismically active part of the buried Southern Alps. Using a combination of magnetostratigraphy and paleosecular variation analysis, we generated an age-depth model for the Monte Netto stratigraphy that encompasses, from the top, Upper Pleistocene (11-72 ka) loess-paleosols overlaying fluvial sediments spanning the Brunhes-Matuyama boundary (773 ka) and the top Jaramillo (990 ka). The identification of the same magneto-chronostratigraphic surfaces in nearby drill cores from regions of the Po Plain not affected by neotectonic deformation allowed estimating a mean rate of tectonic uplift of the hillock relative to the neighboring plain of 11.3±1.5 cm/ka, and an absolute uplift relative to sea level of ~19.3 cm/ka. Finally, our paleomagnetic analyses from the uppermost loess sequence disclosed the complexity of the tectonic evolution of the Monte Netto structure, which shows evidence of a two-phase rotational deformation linked to coseismic surface faulting due to recent seismic activity.

Keywords

Magnetochronology; Pleistocene; paleosecular variations; loess-paleosols; neotectonic deformation; Po Plain.

1 Introduction

The densely anthropized Po Plain of northern Italy is characterized by seismically active buried compressional structures related to the Alps and Apennines fold-and-thrust belts (Fig. 1a; Bigi et al., 1990; Michetti et al., 2012; Livio et al., 2009; 2019). Recent seismic events (since 1985; ISIDe Working Group, 2007) along the southern fringe of the Alps between Lake Iseo and Lake Garda have relatively low seismic releases and shallow crustal depths (10±7 km). These are distinctively clustered in correspondence of anticlines that rise with respect to the surrounding plain forming several isolated morphologies, including the Monte Netto and Castenedolo hillocks near the city of Brescia (Desio, 1965) (Fig. 1b). In the same area, the destructive December 25, 1222 Brescia earthquake (Intensity = IX on MCS [Mercalli-Cancani-Sieberg] scale; Guidoboni and Comastri, 2005) has also been reported and possibly associated to these structures (Livio et al., 2009), thus confirming that this region of the northern Po Plain is characterized by potentially high seismic hazard (e.g., Faccioli, 2013; Vanini et al., 2018).

Here we focus on the Monte Netto tectonic hillock (Fig. 1b) that exposes a complex stratigraphy including, from the top, a sequence of Upper Pleistocene loess and paleosols (LL in Fig. 1c; general stratigraphy in Fig. 2) passing downward to a sequence of fluvial/alluvial sediments (AL in Fig. 1c; Fig. 2) (Zerboni et al., 2015). The Monte Netto hillock is located on top of a major buried reverse fault (Capriano del Colle Backthrust; Fig. 1b-c). The loess-paleosol sequence at the top of the hillock is affected by shallow (and exposed) folding and faulting (Livio et al., 2009, 2014, 2019, 2020) (Fig. 2; see also further below). We combine magnetostratigraphy, paleomagnetic secular variation (PSV) and available optically stimulated luminescence (OSL) dating to develop an age model of deposition of the overall Monte Netto sequence for comparison with coeval magnetostratigraphically-calibrated drill cores from the literature taken in the surrounding Po Plain and not related to neotectonic deformation (see also below). Specifically, our aims are to (i) date the Monte Netto stratigraphic sequence using magnetic polarity reversal boundaries, e.g. the Brunhes-Matuyama boundary and the top Jaramillo, (ii) improve the age modelling in the Late Pleistocene portion of the Brunhes Chron by using a combination of PSV analysis and OSL data, (iii) use magnetic polarity reversal boundaries to correlate the Monte Netto sequence to coeval sequences from the surrounding and largely undeformed plain, (iv) estimate the elevations of such correlative polarity reversal boundaries in order to gauge rates of rock uplift of the Monte Netto structure relative to the surrounding plain, (v) use paleomagnetic data to verify the occurrence of tectonic rotations, and (vi) generate a comprehensive time-calibrated depositional-deformational model of the investigated area, which pertains to a seismically active sector of the densely anthropized Po Plain (Livio et al., 2009) that is under active monitoring for seismic hazard (Vanini et al., 2018).

2 Geology and Stratigraphy

The regional Pleistocene stratigraphy of the Po Plain was investigated in the recent years through a series of drill cores (cores RL1 to RL7 in Fig. 1a; Muttoni et al., 2003; Scardia et al., 2006, 2012; for additional cores not on map, see Scardia et al., 2012) and outcropping sections (e.g., Enza section, Gunderson et al., 2014; Arda section, Monesi et al., 2016; Fig. 1a) that were age-calibrated using magnetostratigraphy through the recognition of the Brunhes-Matuyama boundary, the Jaramillo subchron, and sometimes also the Olduvai subchron. Studies on cores RL1–RL7 revealed that in the late Early Pleistocene, the northern Po Plain was characterized by continental sedimentation in low-energy meandering fluvial systems alternating with occasional marine transgressions during sea level high-stands. Since ~870 ka still in the late Early

Pleistocene, and for the ensuing Middle Pleistocene, sedimentation shifted to high-energy, coarse grained sands and gravels attributed to alluvial fans and braided river systems that rapidly prograded transversally from the Southern Alps and the Apennines onto the Po Plain as the result of the onset of the major Pleistocene glaciations corresponding to marine isotope stage (MIS) 22 at ~870 ka (Muttoni et al., 2003; Scardia et al., 2006).

These studies provide a regional magnetochronologic framework for the Pleistocene evolution of the Po Plain that represents a valuable starting point for the present study aimed at determining the stratigraphic and neotectonic deformation history of the seismogenic Monte Netto structure. The Monte Netto hillock is located at the northern margin of the Po Plain foredeep, along an array of E-W trending thin-skinned blind thrusts belonging to the western sector of the buried Southern Alps (e.g., Livio et al., 2009; Maesano et al., 2015). In particular, Monte Netto is located on top of a N-verging buried reverse fault (Capriano del Colle Backthrust, after Livio et al., 2009; 2014; Fig. 1b-c). The analysis of industrial seismic reflection data highlighted the presence in the study area of growth strata dated from the Pliocene to the Middle Pleistocene, and allowed constraining slip rates of the backthrust as slowing down from 2.5 mm/yr to 0.43 mm/yr since the Pliocene (Livio et al., 2009). The Capriano del Colle Backthrust is also structurally associated with shallower faulting and folding (Livio et al., 2014). At the top of the Monte Netto hillock, fault-related folding of Middle Pleistocene fluvial/alluvial deposits and Upper Pleistocene loess and paleosols is evident from field observations (Figs. 1c, S1; see also below). Incised fluvioglacial sediments attributed to the Last Glacial Maximum characterize the surrounding plain (Fig. 1c).

At Monte Netto, we studied 6 stratigraphically superposed sections, from top to bottom: Cava Danesi Loess, Cava Danesi Fluvial, Top Colle, Salita, Cascina Santus, and Cascina Braga

(Figs. 1d, 2). The Cava Danesi Loess section is located on the eastern wall of an isolated mound at the top of the Monte Netto hillock, to the south of the aforementioned fault-related folding system, where loess strata appear sub-horizontal (Fig. S1). It consists of silty clays interpreted as loess interlayered with paleosols formed under Mediterranean climate conditions (Lehmkuhl et al., 2021), and is arranged in four units from PL1 (top) to PL4 (bottom), each containing in the lower part pedogenetic Mn-Fe nodules or concretions, underlain by unit PL5 of fluvial/fluvioglacial origin (Figs. 2, 3a) (Zerboni et al., 2015). A level in PL2 yielded Mousterian Neanderthal lithics, whereas a level in PL4 yielded older lithics (Fig. 3a; Delpiano et al., 2019). As previously stated, the Cava Danesi Loess section is located immediately to the south of a shallow fault-propagation fold (Fig. S1; Livio et al., 2009; 2019; 2020). The kinematic restoration of the outcropping anticline (Livio et al., 2014; 2020) reveals that this structure is a break-through fault-propagation fold, dipping ca. 24° to the north, that grew while slowing down its propagation-to-slip ratio and finally intersected the topographic surface in the Late Pleistocene, possibly during the Last Glacial Maximum (Livio et al., 2020). The analyzed units display a typical stratigraphic architecture of growth strata across a growing anticline. Close to the exposed fault line, i.e., a few meters to the north of the Cava Danesi Loess section (Fig. S1), units PL5 and PL4 appear affected by synsedimentary folding followed by subsequent faulting, while units PL3 and PL2 overlap the anticline with a significant decrease in thickness. Finally, unit PL1 levels-out the anticline, being only displaced by bending-moment normal faults, on the crest of the anticline (see also Livio et al., 2014; 2020). These normal faults ruptured during repeated surface faulting earthquakes, the last one occurring during the Holocene (Livio et al., 2014). More to the south, where the sampled Cava Danesi Loess section is located, units PL1-PL5 flatten-out and lie sub-horizontally (Fig. S1). The nearby Cava Danesi Fluvial section is composed of fluvial/alluvial silts of unit PL5 and is outcropping below the loess-paleosol sequence, well exposed to the north of the anticline in the backlimb of the growing fault-related fold (Figs. S1, 2).

Stratigraphically below the Cava Danesi Loess and Fluvial sections, and clear of the aforedescribed fault-propagation fold, we sampled the Top Colle section, consisting of yellowish-brown, polygenic, medium-grained fluvial/alluvial sands, and further downward, the Salita section, comprised of sands and polygenic gravels in a sandy matrix, underlain by greyish-brownish silty sands with Ca-carbonate concretions, and laminated yellowish-brown sandy silts (Fig. 2). We also sampled the Cascina Santus section, a lateral equivalent of the Salita section showing similar sedimentary and lithological characteristics, while the lowermost sampled section is Cascina Braga, consisting of medium-fine sands, either well-cemented or unconsolidated, passing downward to polygenic coarse gravels, coarse sands, and greyish- or yellowish-brown silty clay (Fig. 2).

3 Paleomagnetism

3.1 Materials and Methods

A total of 186 oriented core-samples were collected along the 6 stratigraphic sections described above (Fig. 2). Samples were retrieved with a hand-corer or a water-cooled electric drill and have been oriented with a magnetic compass. Cores of typically ~7-8 cm in length were split in two standard-sized ~10cc cylinders. The stratigraphically uppermost Cava Danesi Loess section (Figs. 2, 3) was sampled at high resolution (one core sample every 3-5 cm) to investigate the occurrence of short excursions and paleosecular variations of the Earth's magnetic field. The underlying sections Cava Danesi Fluvial, Top Colle, Salita, Cascina Santus, and Cascina Braga

(Fig. 2) were sampled every 10-20 cm to identify the main magnetic polarity reversals of the Earth's magnetic field (e.g., Brunhes-Matuyama boundary, top Jaramillo).

The initial magnetic susceptibility (k) was measured every centimeter along the Cava Danesi Loess section with a Bartington MS2-K field sensor as well as on the paleomagnetic samples with a Bartington MS2-B sensor. Samples were subjected to thermal demagnetization from room temperature up to ~700°C in steps of 25-50°C with an ASC thermal demagnetizier, and the natural remanent magnetization (NRM) was measured after each temperature step with a 2G Enterprises DC-SQUID cryogenic magnetometer located in a magnetically shielded room. The magnetic component directions were determined through least-square analysis (Kirschvink, 1980). A total of 13 samples were subjected to hysteresis experiments and backfield acquisition curves of isothermal remanent magnetization (IRM) using a vibrating sample magnetometer Microsense EZ7. Hysteresis loops of magnetization [Am^2/kg] *versus* applied field [T] have been used to determine values of coercivity [B_c], saturation magnetization [J_s], and saturation remanence [J_r] after correction for paramagnetic contributions. The parameter coercivity of remanence [B_r] was obtained from IRM backfield acquisition curves performed on the same samples. On four of these samples, low resolution first-order reversal curves (FORCs; Roberts et al., 2000; 2014) were also obtained and interpreted using FORCinel (Harrison and Feinberg, 2008). Finally, four samples were subjected to thermal demagnetization of a three-component IRM (Lowrie, 1990) in fields of 0.12 T, 0.4 T, and 1.5 T using a pulse magnetizer AC IM-10-30. The paleomagnetic analyses were performed at the LASA Paleomagnetics Laboratory.

3.2 Rock-magnetic properties

The low frequency initial magnetic susceptibility of the Cava Danesi Loess section varies between ~150 and ~1500·10^{-6} SI units with generally higher values in the Mn-Fe-enriched lower parts of units PL1-PL4 (Fig. 3b). The mean susceptibility of the underlying fluvial/alluvial silts varies between ~3·10^{-6} SI at the Cava Danesi Fluvial section (unit PL5) and ~900·10^{-6} SI at the Cascina Braga section. Rock-magnetic experiments reveal the occurrence of variable mixtures of magnetite and hematite in the Cava Danesi Loess section and a dominant hematite signal associated with magnetite/maghemite in the fluvial/alluvial silts of the underlying sections. Thermal demagnetization of three component IRM of samples 10 and 84 from the Cava Danesi Loess section (Fig. 4; stratigraphic position of samples in Fig. 3a) shows a signal carried by the 0.12 T curves with a maximum unblocking temperature of ~575°C interpreted as due to the presence of magnetite. The 1.5 T and 0.4 T curves are instead characterized by maximum unblocking temperatures up to ~680°C signaling the presence of hematite. The 1.5 T curve of sample 10 shows also a drastic drop at ~100°C interpreted as goethite. Backfield IRM acquisition experiments on samples 10 and 84 confirm the occurrence of two magnetic phases with contrasting coercivities compatible with magnetite and hematite (Fig. 4, right panels) and characterized by median destructive fields (B1/2) of 10-50 mT and ~1000 mT calculated according to the Gaussian analysis of Kruiver et al. (2001). Hysteresis loops of samples 10 and 84 are wasp-waisted with values of J_r/J_s of ~0.10-0.14 and of B_r/B_c of ~4.5-6.8 that are plotted on a modified Day diagram (Dunlop et al., 2002) (Fig. 5). Similar hysteresis ratio values characterize samples 1, 2, 6, and 15 from the Cava Danesi Loess section. Low-resolution FORC diagrams of samples 10 and 84 (Fig. 5) show asymmetric peaks centered at $B_u \approx 0$ and extending to $B_c \approx 0.02$ T coexisting with higher coercivity tails, which suggests a mixture of single domain

(SD) magnetite and high coercivity hematite/goethite. Divergence from the central ridge could reflect superparamagnetic contributions. A second cluster of samples from the Cava Danesi Loess section displays lower J_r/J_s values on the Day diagram (Fig. 5, samples 23, 33, 49, 65, 87). Sample 23 has a wasp-waisted hysteresis with a FORC slightly more divergent along the vertical B_u axis and with a less developed high coercivity tail along the central ridge, interpreted as signaling the dominance of coarser grained magnetite.

Samples CB7 and CB20 from the fluvial silts of the Cascina Braga section show a dominant hematite signal whereby the 1.5 T and 0.4 T curves are characterized by maximum unblocking temperatures above 600°C (Fig. 4). There are also inflections in the 0.12 T and 0.4 T curves between ~250°C and ~450°C tentatively interpreted as due to maghemite (CB7) and magnetite (CB20). This interpretation is confirmed by the backfield IRM acquisition curves that show an initial low coercivity component (magnetite/maghemite) followed by a higher coercivity component (hematite) (Fig. 4). Hysteresis loops of these samples are less wasp-waisted in shape. Sample CB7 displays J_r/J_s and B_r/B_c values close to values expected for pure hematite (mh 100% on the Day plot of Fig. 5; data from Liu et al., 2019) and a low-resolution FORC with an asymmetric central ridge elongated towards high coercivities that could be compatible with dominant hematite, coexisting with pronounced vertical divergence along the B_u axis that could be due to superparamagnetic contributions. Instead, sample CB20 shows lower J_r/J_s and higher B_r/B_c values, and a FORC central asymmetric swell restricted to low coercivities, more compatible with coarse-grained magnetite/maghemite, in substantial agreement with the IRM experiments.

3.3 Magnetostratigraphy

The thermal demagnetization analyses of the natural remanent magnetization show the presence of a viscous overprint component A of normal polarity, oriented northerly and down, which has been removed between room temperature and a maximum of ~250°C, while the characteristic remanent magnetization (ChRM) component, interpreted as the primary magnetic signal, was detected in 139 samples up to ~580°C-675°C (Fig. 6; demagnetization data in Tab. S1), suggesting that both magnetite and hematite contribute to the ChRM, in agreement with the rock-magnetic experiments. The ChRM component directions are oriented with northerly declinations and downward inclinations, representing normal magnetic polarity, or southerly declinations and upward inclinations representing reverse polarity (Fig. 6). In general, ChRM component directions are well resolved in samples from the Cava Danesi Loess section, where they trend linearly to the origin of the demagnetization axes (8, 53, and 75; Fig. 6), whereas in the other fluvial-dominated sections they tend to be more scattered, sometimes forming clusters before final unblocking at high temperatures (e.g., F1 from Cava Danesi Fluvial, MNTC05 from Top Colle, MNS04 from Salita, CSA01, CSB05, CSC02 from Cascina Santus, and CB23, CB27 and CB3 from Cascina Braga; Fig. 6). Standard Fisher statistics yielded an overall mean ChRM component direction for the Cava Danesi Loess section at Dec = 1.3°E, Inc = 51.5° (k = 25, α_{95} = 3.1, n = 88) (Fig. 7a, upper stereonet) and for the fluvial (pre-loess) sequence (Cava Danesi Fluvial, Top Colle, Salita, Cascina Santus, and Cascina Braga) at Dec = 5.9°E, Inc = 49.7° (k = 13, α_{95} = 5.7°, n = 51) (Fig. 7b). No tectonic correction was applied as bedding attitudes in all sampled sections appear close to horizontal.

The normal polarity ChRM record of the Cava Danesi Loess section shows high-frequency variability in declination and inclination (Fig. 3c, d) that is relatively well-defined with maximum angular deviation (MAD) errors generally lower than 10° (Fig. 3e). Notably, the declination values oscillate along a long-term trend of 0.091°/cm with easterly declinations in the lower part of the section, northerly declinations in the mid part, and westerly declinations in the upper part (red line with 95% error envelope in Fig. 3c). The inclination values show instead a more modest long-term increase trend of 0.025°/cm moving up-section (Fig. 3d). We will return on the meaning of these trends, which we interpret as mainly due to tectonic deformation (declination trend) and compaction (inclination trend).

The ChRM component directions have been used to calculate virtual geomagnetic pole (VGP) latitudes (Tab. S2). These results have been used to determine the position in the overall Monte Netto sequence of the Brunhes-Matuyama boundary and the top Jaramillo (Fig. 2). These data were used in conjunction with OSL dates and PSV analysis for sedimentation age modelling and assessments of rates of tectonic uplift and deformation of the Monte Netto structure.

4 Age model of deposition

The Cava Danesi Loess section at the top of the Monte Netto stratigraphy is of homogeneous normal polarity (Figs. 2, 3). The OSL dates, ranging from 19.9±2.3 ka in PL1 to 44.4±5.4 ka in PL2 (Fig. 3a; Zerboni et al. 2015), indicate a late Brunhes age for the sequence. No short polarity excursions, such as the Laschamp (41 ka) or the Blake (115 ka), have been found. To improve the chronological constrains based on the available OSL ages, which have rather large uncertainties, we interpret the high-frequency variability in ChRM declination observed in the Cava Danesi Loess section as PSV and use this record for correlation to a dated PSV record close to our study area (Liu et al., 2020; see below). PSV is best resolved in high sediment accumulation rate records such as marine sediments with sedimentation rates above ~20 cm/ka, even though records with lower sedimentation rates are commonly adopted for so-called smoothed PSV estimates (e.g., Panovska et al., 2017). In the Cava Danesi Loess section, OSL dates in unit PL1 at 19.9±2.3 ka and 24.6±2.9 ka separated by 20 cm of section (Fig. 3a) suggest accumulation rates that could fall in the suitable range for at least smoothed PSV determination.

For PSV analysis, the long-term declination trend of 0.091°/cm (interpreted as due to tectonic deformation; see below) has been subtracted by linear detrending (Fig. S2a). The inclinations have also been corrected for the observed minor long-term trend of 0.025°/cm (Fig. S2b). This inclination trend could be interpreted as due to compaction, with lower levels characterized by slightly shallower mean ChRM inclinations than inclinations in upper levels. The detrended ChRM declination/inclination record has subsequently been tested for additional (residual) sedimentary inclination flattening using the Elongation/Inclination (E/I) method of Tauxe and Kent (2004). A flattening factor f = 0.86 was obtained (Fig. S3) and applied to further correct the (detrended) ChRM inclination record (Fig. S2c). To verify that the corrected (detrended and unflattened) declination-inclination record from the Cava Danesi Loess section indeed reflects PSV, the value of VGP scatter S' (Tauxe and Kent 2004), representing the angular standard deviation of the scatter of the VGPs with latitude, was calculated. The obtained value of S' = 15.46 was subsequently corrected for within-site scatter, obtaining a value of S_f = 15.44 (McElhinny and McFadden, 1997) that was compared with the values of the GAD field model TK03 of Tauxe and Kent (2004) and the global PSV record MM97 of McElhinny and McFadden (1997) at the Monte Netto latitude, finding excellent agreement especially with MM97 (Fig. 8, Tab. S3).

For age modelling, the detrended declination record of the Cava Danesi Loess sequence with ±MAD error envelope was correlated to the high-resolution PSV record of Liu et al. (2020) from a stack of 16 sediment cores recovered from the Black Sea and dated between 14.5 ka and

68.9 ka using radiocarbon dating and correlations to the Pleistocene global climate record (Fig. 9). PSV records from locations closer to the study area, e.g. in the in the Adriatic sea, have not been taken into consideration because confined to the Holocene (Vigliotti, 2006). We opted to use directional data for correlation and age modelling instead of relative paleointensity derived from rock magnetic data because of the complex and variable mineralogical content of the studied sediments. The Black Sea record, which is of much higher resolution than the Monte Netto record, was smoothed using a LOESS (*locally weighted running line smoother*) function with smoothing factor of 0.02 (Fig. 9). The two curves have then been compared and correlated considering the main declination peaks (values of at least 20° east or west of north) bracketed between OSL ages while considering also the occurrence of reductions in sedimentation rate and/or unconformities between individual loess units (interglacial/interstadial gaps in sedimentation and/or phases of pedogenesis). A total of 17 age-depth values obtained from the Cava Danesi Loess-Black Sea PSV peak-to-peak correlation (input values in Tab. S4) were used for the construction of a deterministic age-depth model of deposition (Lougheed and Obrochta, 2019). The OSL dates have been used as a benchmark to drive the PSV correlation but did not enter the final age model because of their large uncertainties that may encompass sedimentary gaps between loess units. The occurrence of such gaps explains for example the absence in the Cava Danesi Loess section of the Laschamp polarity excursion (~41 ka), which is expected to occur considering the overall age span of the correlated records, but it has not been recorded most probably because it falls in the interval of reduced deposition/unconformity at the PL1-PL2 boundary (Fig. 9).

The final age-depth model (Fig. 10) has been run with 10^5 iterations using xfactor = 0.2 (Lougheed and Obrochta, 2019) evaluated according to the density of ages along the sequence.

These parameters were chosen after several simulations as representing the best approximation of the geological-depositional history of the sequence including the occurrence of unconformities (gaps) between loess units (Fig. 9). This deterministic age-depth model yielded interpolated ages (with 95% uncertainty) of the stratigraphic levels constituting the Cava Danesi Loess sequence including estimates of the duration of the gaps or intervals of reduced sedimentation between individual loess units (Fig. 10; output values in Tab. S4). According to our age model, loess units PL1-PL3 deposited between 16.4 ka and 67.0 ka at variable sediment accumulation rates. For completeness, we linearly extrapolated the age model up to the top of PL1, obtaining an age of 11 ka, and down to the base of PL3, obtaining an age of 72 ka (red dashed line in Fig. 10). Ages of units PL4 and PL5 have not been modelled because of lack of tie-points. For actual sedimentation rates assessment, we subdivided the age model in 7 linear segments, estimating an average accumulation rate for each segment (Fig. 10). According to this analysis, accumulation rates resulted varying between a maximum of 30.6±1.7 cm/ka in PL2 and a minimum of 1.7±0.007 cm/ka in PL1, as reported in Figure 10. Some of these values are low for optimal PSV determination but relatively adequate for smoothed PSV estimates (see e.g., Panovska et al., 2017). Finally, according to this model the Mousterian archaeological level in unit PL2 has an age of 43.4±0.4 ka, while the age of the underlying archaeological level in PL4 is >72 ka (Fig. 10).

The fluvial sediments below the Cava Danesi Loess sequence have been dated using main magnetic polarity reversals. The Brunhes (C1n) normal polarity record observed at Cava Danesi Loess and nearby Cava Danesi Fluvial sections extends downward into the Top Colle section (Fig. 2). The underlying sections Salita and Cascina Santus show a well-expressed reverse polarity record attributed to the Matuyama Chron (C1n.1r), while the lowermost section

Cascina Braga shows consistent normal polarity interpreted as a partial record of the Jaramillo subchron (C1r.1n) (Fig. 2). The Brunhes-Matuyama boundary falls in a stratigraphic gap of ~5 m due to lack of exposed sediments. Assuming an age of 773 ka for the Brunhes-Matuyama boundary and of 990 ka for the top Jaramillo (Channell et al., 2020), the long-term sedimentation rate of the fluvial (pre-loess) sequence is estimated at ~2.8±2 cm/ka assuming no major sedimentary hiata between individual lithological units and taking into account the stratigraphic gap across the Brunhes-Matuyama boundary. We stress that alternative ages of 780 ka or 781 ka for the Brunhes-Matuyama boundary (see discussion in Channell et al., 2020) would have the effect to increase average sedimentation rates by ~3%.

5 Tectonic implications

5.1 Long-term uplift of the Monte Netto structure

The long-term deformation history of the Monte Netto structure due to the activity of the Capriano del Colle Backthrust can be investigated comparing the elevations of levels that registered the Brunhes-Matuyama boundary and the top Jaramillo in sections from the study area and in two drill cores from the surrounding Po Plain (RL1 Ghedi and RL2 Pianengo; Scardia et al., 2006; Muttoni et al., 2003) that are not associated with tectonic deformation (Fig. 11; for locations of cores, see Fig. 1a). The vertical displacement of the Brunhes-Matuyama boundary between Monte Netto and RL1 is of 68.5±4.8 m, and between Monte Netto and RL2 is 78±10.3 m. Similarly, the displacement of the top Jaramillo at Monte Netto is of 130.9±2.6 m relative to RL1 and of 129.4±2.1 m relative to RL2 (Fig. 11). Neglecting the relatively minor differences, which could be due to local and undetected variations in sediment accumulation rates, such displacements indicate an average rate of vertical tectonic uplift of the Monte Netto hillock relative to the surrounding plain of 11.3±1.5 cm/ka calculated since the Brunhes-Matuyama boundary (773 ka; *terminus post quem*). This long-term tectonic uplift is related to the activity of the buried Capriano del Colle Backthrust, observed in seismic profiles at a depth of 2-3 km (Livio et al., 2009) under the Monte Netto uplifted stratigraphic sequence (CCB in Fig. 11, depth not to scale; see also figure 4 in Livio et al., 2009).

This rate of local tectonic uplift is superposed to a rate of regional uplift of the northern Po Plain relative to sea-level as observed in several Pleistocene drill cores (RL1-RL7, Fig. 1a). Scardia et al. (2006; 2012) used magnetochronology from these cores to assess the age of transitional marine (beach, shoreface) facies marking sea level, which were found to punctuate the stratigraphic record repeatedly between 1240 ka (MIS 37) and 850 ka (MIS 21). After applying a simple Airy isostatic correction to account for sediment loading, they found that in all analyzed cores (except for core RL2 Pianengo, see below), these transitional facies presently lie ~70-120 m above maximum Pleistocene sea levels of corresponding ages, implying a generalized phase of uplift of the northern Po Plain relative to sea level that occurred since the deposition of the youngest displaced transitional deposits of late Early Pleistocene age (Scardia et al., 2006; 2012). In core RL1 Ghedi, this uplift relative to sea level was estimated at ~8 cm/ka since ~870 ka, while core RL2 Pianengo required no uplift correction to restore the transitional facies on the reference sea level curve, possibly because of a preceding phase of local subsidence that resulted in a final null net difference (Scardia et al., 2006; 2012 for additional information). In any case, assuming coherence between Monte Netto and core RL1 Ghedi, the total uplift rate of Monte Netto relative to sea level since the late Early Pleistocene (sum of local tectonic uplift plus regional isostatic uplift) is of ~19.3 cm/ka (Fig. 11), in substantial agreement with previous assessments (Livio et al., 2009).

5.2 Rotational deformation of the loess sequence

A close inspection of the ChRM component directions reveals that the Cava Danesi Loess section is affected by a recent phase of complex rotational deformation presumably related to surface faulting and folding. Recall that the undetrended (i.e., as measured) ChRM declination record of the Cava Danesi Loess section oscillates around a long-term trend that is displaced relative to the true north direction (Fig. 3c, red line), with ChRM directions pointing on average ~15°E (=15° east of north) at the base of the sequence and 345°E at the top. A statistically significant difference of ~25°±11° is revealed by Fisher statistics applied to n=20 ChRM directions from the lowermost 60 cm of the loess sequence relative to n=20 directions from the uppermost 60 cm of the same sequence (Fig. 7a, lower stereonet). Considering that both these 60 cm-thick subsections should cover about 10 ka of sedimentation according to the age model of Figure 10, the observed difference in mean declination cannot be explained as due to PSV alone, leaving tectonic rotation as the only plausible contributing factor to explain the observed declination trend. Instead, the Cava Danesi Fluvial section, stratigraphically below the loess, is characterized by 6 north-pointing ChRM declinations (Fig. 3c, d). No statistically significant rotation was observed also in the other pre-loess fluvial sections (Top Colle, Salita, Cascina Santus, Cascina Braga; Fig. 7b). Recall also that the Cava Danesi Loess section is located immediately to the south of a fault-propagation fold (Fig. 12A and S1) (Livio et al., 2014; 2020), where some deformation is expected during fold growing. Conversely, the (non-rotated) Cava Danesi Fluvial section is located in the backlimb of the same fault system, where simple translation is expected (Fig. S1).

We applied the age model described above to transform the undetrended ChRM declination values of the Cava Danesi Loess section (Fig. 3c) from depth (cm) to time (ka) coordinates, and we attempt to explain this dated record using a simple two-stage rotational deformation model. According to our model, the loess sequence experienced an initial long-term phase of syn-depositional vertical-axis clockwise (cw) tectonic rotation at rates of 0.43°±2.5°/ka (error bound on rotation rate derived from error bound on declination trend of Fig. 3c) from ~72 ka (age of the oldest ChRM directions) up to ≤11 ka (age of the youngest ChRM directions). In this way, the oldest ChRM directions should be affected by maximum eastward displacements and the youngest directions should be non-rotated (Fig. 12b). We cannot assess precisely when this rotation ended in the 11-0 ka interval (Fig. 12b). This rotational phase appears progressive (syn-depositional) at least at the time scale of the observation and is mainly due to a diverse tendency of the fault to propagate upwards, as also attested in Livio et al. (2020). According to observations on two profiles of the same fault-propagation fold exposed along the eastern and western walls of the Monte Netto mound (Fig. 12a), the fault tip propagation was more inhibited in the east, resulting in a more pronounced folding and tilting of the front-limb sector that, as a consequence, generated the observed progressive clockwise rotation of the Cava Danesi Loess section.

Subsequently, we record a second phase of deformation resulting in a single pulse of rigid-body rotation of the entire Cava Danesi Loess section around a vertical axis to yield the actual configuration (Fig. 12c). This latter deformation phase could be associated with the surface emergence of the fault, to the west, while in the eastern sector fault tip propagation was still inhibited (Fig. 12c). The lack of distributed deformation from the emergence of the fault onwards resulted in a more pronounced front advancement to the west, and, in turn, an anticlockwise cumulative rotation of 15-19° (Fig. 12c). According to the available record, this phase of rotation occurred after 11 ka. It is noteworthy that a similar age for the fault emergence was supposed by Livio et al. (2020) based on the age constraints then available.

Alternative mechanisms to explain the Cava Danesi Loess declination record involving deeper deformation and rotation (e.g., due to the deep Capriano del Colle Backthrust) are excluded, so far, by considering that the Cava Danesi Fluvial section, as well as the other fluvial sections from the Monte Netto stratigraphy (Top Colle, Salita, Cascina Braga, Cascina Santus), located outside the expected deformation zone of the shallow fault-propagation fold, appear non-rotated.

6 Conclusions

We used magnetostratigraphy in conjunction with PSV analysis to interpret quantitatively the Pleistocene tectono-stratigraphic evolution of the Monte Netto hillock, a seismically active structure in the anthropized and vulnerable Po Plain of northern Italy. Our analysis allowed to reach the following conclusions:

- The Monte Netto stratigraphy contains a record of the Brunhes-Matuyama boundary and the top Jaramillo that can be correlated to coeval records previously recognized in drill cores from the surrounding undeformed plain.
- According to these correlations, the Monte Netto structure is uplifting relative to the neighboring undeformed plain at a mean rate of 11.3±1.5 cm/ka since the late Early Pleistocene. This local component of tectonic uplift is linked to the long-term activity of the Capriano del Colle Backthrust, located 2-3 km below the uplifted Monte Netto stratigraphy (Fig. 11).

- Taking into account a previously recognized component of regional isostatic uplift of the northern Po Plain relative to sea level, we established that the Monte Netto structure is uplifting relative to sea level at a mean rate of ~19.3 cm/ka since the late Early Pleistocene.
- The loess sequence at the top of the Monte Netto structure contains a smoothed PSV record useful for sedimentation rate modelling when correlated to the dated PSV record from the Black Sea of Liu et al. (2020). The loess record deposited from 11 ka to at least 72 ka. Notably, our PSV-based chronology of loess deposition is in principle applicable to other loess sequences from the Eurasian loess basin.
- The Monte Netto PSV record revealed also that the loess sequence is affected by a complex history of recent rotational deformation. This is comprised of a first phase of clockwise rotation at a mean rate of 0.43°/ka between ~72 ka and ≤11 ka, and a subsequent phase of 15-19° counter-clockwise after 11 ka. Both rotational phases were linked to the activity of surface faulting, and modelled taking into account fault geometries and kinematics.
- These data, in conjunction with the historical record of shallow crustal earthquakes (ISIDe Working Group, 2007), suggest that Monte Netto and similar tectonic structures from the Po Plain should be monitored for hazard prevention (Vanini et al., 2018).

Acknowledgments

We thank the Associate Editor Jaime Urrutia Fucugauchi and Reviwers Augusto Rapalini and Manuel Calvo for very insightful comments that helped improve this manuscript. We also thank the municipality of Capriano del Colle and the Fornaci Laterizi Danesi S.p.A. for support and permission to access the site. This research has been funded by Project CARG Geological Map of Italy, sheet Brescia 1: 50,000 (PI Gianluca Norini, CNR-IGAG). Additional financial support came from project CTE_NAZPR19AZERB_01 entrusted to AZ. Part of this study is supported by the Italian Ministry of Education, University and Research (MIUR) through the project 'Dipartimenti di Eccellenza 2018–2022' (DECC18_020_DIP) awarded to the Dipartimento di Scienze della Terra 'A. Desio' of the University of Milano.

References

Bigi, G., Cosentino, D., Parotto, M., Sartori, R., and Scandone, P., 1990, Structural model of Italy: Firenze, Società Elaborazioni Cartografi che (S. EL.CA.), Consiglio Nazionale della Ricerche Progetto Finalizzato Geodinamica, scale 1:500,000, 9 sheets.

Channell, J.E.T., Singer, B.S., Jicha, B.R., 2020. Timing of Quaternary geomagnetic reversals and excursions in volcanic and sedimentary archives. Quaternary Science Reviews 228 (2020), 106114. https://doi.org/10.1016/j.quascirev.2019.106114.

Delpiano, D., Peresani, M., Bertola, S., Cremaschi, M., Zerboni, A., 2019. Lashed by the wind: short-term Middle Palaeolithic occupations within the loess-palaeosoil sequence at Monte Netto (Northern Italy). Quaternary International 502 (2019) 137–147. https://doi.org/10.1016/j.quaint.2019.01.026.

Desio, A., 1965. I rilievi isolati della Pianura Lombarda ed i movimenti tettonici del Quaternario. Rendiconti dell'Istituto Lombardo Accademia di Scienze e Lettere, 99, 881-894.

Dunlop, D.J., 2002. Theory and application of the Day plot (M_{rs}/M_s versus H_{cr}/H_c) 1. Theoretical curves and tests using titanomagnetite data. Journal of Geophysical Research, vol. 107, no. B3. https://doi.org/10.1029/2001JB000486.

Faccioli, E., 2013. Recent evolution and challenges in the Seismic Hazard Analysis of the Po Plain region, Northern Italy. Bull Earthquake Eng (2013) 11:5-33. https://doi.org/10.1007/s10518-012-9416-1.

Guidoboni, E., Comastri, A., 2005. Catalogue of earthquakes and tsunamis in the Mediterranean area from the 11th to the 15th century. Istituto Nazionale di Geofisica e Vulcanologia - Storia Geofisica Ambiente, Roma-Bologna, 1037 p.

Gunderson, K.L., Pazzaglia, F.J., Picotti, V., Anastasio, D.A., Kodama, K.P., Rittenour, T., Frankel, K.F., Ponza, A., Berti, C., Negri, A., Sabbatini, A., 2014. Unraveling tectonic and climatic controls on synorogenic growth strata (Northern Apennines, Italy). Geological Society of America Bulletin. https://doi.org/10.1130/B30902.1.

Hammer, Ø., Harper, D.A.T., Ryan, P.D., 2001. Past: paleontological statistics software package for education and data analysis. Palaeontologia Electronica 4 (1) art. 4: 9pp.

Harrison, R.J., Feinberg, J.M., 2008. FORCinel: An improved algorithm for calculating first-order reversal curve distributions using locally weighted regression smoothing, Geochem. Geophys. Geosyst., 9, Q05016. https://doi.org/10.1029/2008GC001987.

ISIDe Working Group,2007. Italian Seismological Instrumental and Parametric Database (ISIDe). Istituto Nazionale di Geofisica e Vulcanologia. https://doi.org/10.13127/ISIDE.

Kirschvink, J.L., 1980. The least-squares line and plane and the analysis of palaeomagnetic data. Geophysical Journal International (1980) 62, pp. 699-718. https://doi.org/10.1111/j.1365-246X.1980.tb02601.x.

Kruiver, P.P., Dekkers, M.J., Heslop, D., 2001. Quantification of magnetic coercivity components by the analysis of acquisition curves of isothermal remanent magnetisation. Earth and Planetary Science Letters, vol. 189, pp. 269-276.

Lehmkuhl, F., Nett, J.J., Pötter, S., Schulte, P., Sprafke, T., Jary, Z., Antoine, P., Wacha, L., Wolf, D., Zerboni, A., Hošek, J., Marković, S.B., Obreht, I., Sümegi, P., Veres, D., Zeeden, C., Boemke, B, Schaubert, V., Viehweger, J., Hambach, U., 2021. Loess landscapes of Europe – mapping, geomorphology and zonal differentiation. Earth-Science Reviews 215, 103496.

Liu, J., Nowaczyk, N. R., Panovska, S., Korte, M., Arz, H. W., 2020. The Norwegian-Greenland Sea, the Laschamps, and the Mono Lake excursions recorded in a Black Sea sedimentary sequence spanning from 68.9 to 14.5 ka. Journal of Geophysical Research: Solid Earth, 125, e2019JB019225. https://doi.org/10.1029/2019JB019225.

Liu, P., Hirt, A.M., Schüler, D., Uebe, R., Zhu, P., Liu, T., Zhang, H., 2019. Numerical unmixing of weakly and strongly magnetic minerals: examples with synthetic mixtures of magnetite and hematite. Geophysical Journal International 217, pp. 280–287. https://doi.org/10.1093/gji/ggz022.

Livio, F. A., Berlusconi, A., Michetti, A.M., Sileo, G., Zerboni, A., Trombino, L., Cremaschi, M., Mueller, K., Vittori, E., Carcano, C., Rogledi, S. 2009. Active fault-related folding in the epicentral area of the December 25, 1222 (Io = IX MCS) Brescia earthquake (Northern Italy): Seismotectonic implications. Tectonophysics (2009) 476, pp. 320–335. https://doi.org/10.1016/j.tecto.2009.03.019.

Livio, F. A., Berlusconi, A., Zerboni, A., Trombino, L., Sileo, G., Michetti, A.M., Rodnight, H., Spötl, C., 2014. Progressive offset and surface deformation along a seismogenic blind thrust in the Po Plain foredeep (Southern Alps, Northern Italy). Journal of Geophysical Research Solid Earth, 119, 7701–7721, https://doi.org/10.1002/2014JB011112.

Livio, F.A., Kettermann, M., Reicherter, K., Urai, J. L., 2019. Growth of bending-moment faults due to progressive folding: Insights from sandbox models and paleoseismological implications. Geomorphology 326 (2019), 152–166. https://doi.org/10.1016/j.geomorph.2018.02.012.

Livio, F. A., Ferrario, M. F., Frigerio, C., Zerboni, A., & Michetti, A. M., 2020. Variable fault tip propagation rates affected by near-surface lithology and implications for fault displacement hazard assessment. Journal of Structural Geology, *130*, 103914.

Lougheed, B.C., Obrochta, S. P., 2019. A rapid, deterministic age- depth modeling routine for geological sequences with inherent depth uncertainty. Paleoceanography and Paleoclimatology, 34, 122–133. https://doi.org/10.1029/2018PA003457.

Lowrie, W., 1990. Identification of ferromagnetic minerals in a rock by coercivity and unblocking temperature properties. Geophysical Research Letters 17 (2), 159-162.

Maesano, F.E., D'Ambrogi, C., Burrato, P., Toscani, G., 2015. Slip-rates of blind thrusts in slow deforming areas: examples from the Po Plain (Italy). Tectonophysics, 643, 8-25.

McElhinny, M.W., McFadden, P.L., 1997. Palaeosecular variation over the past 5 Myr based on a new generalized database. Geophysical Journal International, 131 (1997), 240-252.

Michetti A.M., Giardina F., Livio F., Mueller K., Serva L., Sileo G., Vittori E., Devoti R., Riguzzi F., Carcano C., Rogledi S., Bonadeo L., Brunamonte F., Fioraso G., 2012. Active compressional tectonics, Quaternary capable faults, and the seismic landscape of the Po Plain (N Italy). Annals of Geophysics, 55 (5), 969-1001, doi: 10.4401/ag-5462.

Monesi, E., Muttoni, G., Scardia, G., Felletti, F., Bona, F., Sala, B., Tremolada, F., Francou, C., Raineri, G., 2016. Insights on the opening of the Galerian mammal migration pathway from magnetostratigraphy of the Pleistocene marine-continental transition in the Arda River section (northern Italy). Quaternary Research, 86 (2016), 220-231. https://doi.org/10.1016/j.yqres.2016.07.006.

Muttoni, G., Carcano, C., Garzanti, E., Ghielmi, M., Piccin, A., Pini, R., Rogledi, S., Sciunnach, D., 2003. Onset of major Pleistocene glaciations in the Alps Geology (2003) 31 (11): 989–992. https://doi.org/10.1130/G19445.1.

Roberts, A. P., Pike, C.R., Verosub, K.L., 2000. First-order reversal curve diagrams: a new tool for characterizing the magnetic properties of natural samples. Journal of Geophysical Research 2000, vol. 105, no. B12, pages 28,461-28,475. https://doi.org/10.1029/2000JB900326.

Roberts, A. P., Heslop, D., Zhao, X., Pike, C.R., 2014. Understanding fine magnetic particle systems through use of first-order reversal curve diagrams. Reviews of Geophysics 52, 557–602. https://doi.org/10.1002/2014RG000462.

Scardia, G., Muttoni, G., Sciunnach, D., 2006. Subsurface magnetostratigraphy of Pleistocene sediments from the Po Plain (Italy): Constraints on rates of sedimentation and rock uplift. Geological Society of America Bulletin, November/December 2006, v. 118, no. 11/12, p. 1299–1312, https://doi.org/10.1130/B25869.1.

Scardia, G., De Franco, R., Muttoni, G., Rogledi, S., Caielli, G., Carcano, C., Sciunnach, D., Piccin, A., 2012. Stratigraphic evidence of a Middle Pleistocene climate-driven flexural uplift in the Alps. Tectonics 2012, v. 31, issue 6. https://doi.org/10.1029/2012TC003108.

Tauxe, L., Kent, D.V., 2004. A Simplified Statistical Model for the Geomagnetic Field and the Detection of Shallow Bias in Paleomagnetic Inclinations: Was the Ancient Magnetic Field Dipolar? Geophysical Monograph Series 145. https://doi.org/10.7916/D81N89JT.

Tauxe, L., Shaar, R., Jonestrask, L., Swanson-Hysell, N.L., Minnett, R., Koppers, A.A.P., Constable, C.G., Jarboe, N., Gaastra, K., Fairchild, L., 2016. PmagPy: software package for paleomagnetic data analysis and bridge to the Magnetics Information Consortium (MagIC) Database. Geochemistry, Geophysics, Geosystems 17 (6), 2450-2463. https://doi.org/10.1002/2016GC006307.

Vanini, M., Corigliano, M., Faccioli, E., Figini, R., Luzi, L., Pacor, F., Paolucci, R., 2018. Improving seismic hazard approaches for critical infrastructures: a pilot study in the Po Plain. Bull Earthquake Eng (2018) 16:2529-2564. https://doi.org/10.1007/s10518-017-0102-1.

Vigliotti, L., 2006. Secular variation record of the Earth's magnetic field in Italy during the Holocene: constraints for the construction of a master curve. Geophysical Journal International (2006) 165, 414–429. https://doi.org/10.1111/j.1365-246X.2005.02785.x.

Zerboni, A., Trombino, L., Frigerio, C., Livio, F., Berlusconi, A., Michetti, A. M., Rodnight, H., Spötl, C., 2015. The loess-paleosol sequence at Monte Netto: a record of climate change in the Upper Pleistocene of the central Po Plain, northern Italy. J Soils Sediments (2015) 15:1329–1350. https://doi.org/10.1007/s11368-014-0932-2.

Figures Captions

Figure 1. (a) Structural map of the Po Plain of northern Italy with location of the Monte Netto hillock, as well as of key drill cores from the literature: Ghedi RL1, Pianengo RL2, Cilavegna RL3, Agrate RL4, Trezzo RL5, Cremignane RL6, Palosco RL7 (Scardia et al., 2006, 2012)**.** Also indicated are the locations of Pleistocene magnetostratigraphic sections from the literature discussed in the text: Arda (Monesi et al., 2016), and Enza (Gunderson et al., 2014); (b) shaded relief model of the Monte Netto and nearby Castenedolo hillocks with traces of main buried thrusts (after Livio et al 2009), including the Capriano del Colle Backthrust; (c) geological sketch map of the Monte Netto area and (d) GoogleEarth™ 3D image of the Monte Netto hillock with location of the sampling areas.

Figure 2. Stratigraphic scheme of the Monte Netto hillock based on the six lithological logs studied for magnetostratigraphy placed with respect to meters above sea level. From top (youngest) to bottom (oldest), the sampled sections are: Cava Danesi Loess, Cava Danesi Fluvial, Top Colle, Salita, Cascina Santus, and Cascina Braga. Also shown is a picture of the Cava Danesi outcrop area with location of sampled sections (Cava Danesi Loess, Cava Danesi Fluvial) relative the normal fault system dissecting the sequence (Livio et al., 2009). Samples for paleomagnetism are listed next to the logs and those that gave reliable results were used to establish a magnetic polarity stratigraphy (black squares for normal polarity and white squares for reverse polarity) for correlation to the geomagnetic polarity time scale of the Pleistocene of Channell et al. (2020).

Figure 3. (a) Stratigraphic log of the Cava Danesi Loess section with position of samples collected for magnetostratigraphy and of samples that yielded OSL ages (Zerboni et al., 2015).

Also reported is the Cava Danesi Fluvial section. Paleomagnetic properties are as follows: (b) initial magnetic susceptibility, (c) values of Declination and (d) Inclination of the characteristic remanent magnetization (ChRM) component, and (e) maximum angular deviation (MAD) of the ChRM. The Cava Danesi Loess section is characterized by an evident trend in declination values (c) due to tectonic deformation (see text for discussion). The red lines in (c) and (d) represent the linear best fits with 95% error bounds.

Figure 4. Thermal decay of a three component IRM acquired in fields of 1.5 T, 0.4 T and 0.12 T, and isothermal remanent magnetization (IRM) backfield acquisition curves, of representative samples from the Cava Danesi Loess section (10 and 84) and from the Cascina Braga fluvial sediments (CB7 and CB20). Unblocking temperatures and IRM coercivities are consistent with the occurrence of variable mixtures of essentially magnetite and hematite, as testified also by the wasp-waisted shapes of the hysteresis loops obtained on the same samples (Fig. 5).

Figure 5. Hysteresis loops, corrected for paramagnetic components, and FORC diagrams of selected samples from the Cava Danesi Loess section (10, 23 and 84) and the Cascina Braga fluvial sediments (CB7 and CB20). The central-right panel represents a modified Day plot (Dunlop et al., 2002) of J_r/J_s *versus* B_r/B_c for 12 samples from the Cava Danesi Loess sequence (black dots) and the Cascina Braga fluvial sediments (black diamonds). The theoretical curves of Dunlop et al. (2002) for single domain-10nm superparamagnetic (SD-SP) magnetite mixtures, single domain-multidomain (SD2-MD2) magnetite mixtures, and multidomain (MD) magnetite are also reported for reference together with the magnetite-hematite (mh) mixing curve of Liu et al. (2019) (in blue). See text for discussion.

Figure 6. Vector end-point demagnetization diagrams of representative samples from Monte Netto indicating characteristic remanent magnetization (ChRM) component directions of normal polarity, with northernly declinations and positive (downward) inclinations, or reverse polarity, with southernly declinations and negative (upward) inclinations. Closed symbols are projections onto the horizontal plane and open symbols onto the vertical plane in geographic coordinates. No tilt correction has been applied as bedding is sub-horizontal. Demagnetization steps are expressed in °C.

Figure 7. Equal-area projections of the characteristic remanent magnetization (ChRM) component directions for (a) all samples from the Cava Danesi Loess sequence as well as a selection of n=20 ChRM directions for the base and top of the same loess sequence showing differential tectonic rotations, and (b) samples from the underlying fluvial/alluvial (pre-loess) sequence from sections Cava Danesi Fluvial, Top Colle, Salita, Cascina Santus, and Cascina Braga. Closed symbols are projection onto the lower hemisphere while open symbols onto the upper hemisphere. The stars represent the Fisher mean directions and associated cones of 95% confidence.

Figure 8. Curve of the VGP scatter value *S'* (°) as a function of latitude λ (°) for the statistical GAD model TK03 (Tauxe and Kent, 2004) and the global MM97 record (McElhinny and McFadden, 1997). The red square represents the VGP scatter value corrected for the within-site scatter (S_f=15.44) calculated for the Cava Danesi Loess section.

Figure 9. Correlation of the ChRM declination record of the Cava Danesi Loess section to the dated declination record from the Black Sea of Liu et al. (2020). The ChRM declination record of Cava Danesi (red line) is associated with ± MAD error bounds (blue lines). The Black Sea ChRM declinations have been recalculated via Virtual Geomagnetic Poles (VGP) latitudes and longitudes to Monte Netto coordinates, and smoothed with a *LOESS* function (using the software PAST; Hammer et al., 2001) with a smoothing factor of 0.02 (red lines representing mean smoothed values and blue lines representing $\pm\alpha_{95}$ confidence envelope). The major peaks (values of at least 20° east or west of north) have been correlated (black dashed lines) using as general guidelines the available OSL ages from the Cava Danesi Loess sequence (green boxes and lines). Geomagnetic excursions recorded in the Black Sea record (Norwegian-Greenland Sea, Laschamp and Mono Lake) are reported in blue. The correlation highlighted the absence in the Cava Danesi Loess section of the Mono Lake (~34.5 ka) and Laschamp (~41 ka) polarity excursions due to very low sedimentation rates or pedogenetic *hiata* in the basal parts of units PL1 and PL2, respectively (green boxes).

Figure 10. Age model of deposition of the Cava Danesi Loess section computed using software Undatable (Lougheed and Obrochta, 2019) with input and output age-depth data reported in Tab. S4. Units PL1-Pl3 deposited between 11 ka and 72 ka (see text for discussion).

Figure 11. Magnetostratigraphic correlations between Monte Netto and nearby drill cores RL1 Ghedi and RL2 Pianengo (Scardia et al., 2006; Muttoni et al., 2003) plotted in a common topographic-altimetric reference frame. The Monte Netto structure appears to have undergone a tectonic uplift relative to RL1 and RL2 of 11.3±1.5 cm/ka since 773 ka (*terminus post quem*) due

to the activity of the buried Capriano del Colle Backthrust (CCB), located at a depth of 2-3 km (not to scale in figure) under the uplifted Monte Netto stratigraphy. In addition, core RL1 was previously shown to be characterized by a regional isostatic uplift of ~8 cm/ka relative to sea level, similarly to other cores from the Po plain (Scardia et al., 2006, 2012). The total uplift rate of the Monte Netto structure relative to sea level is therefore of ~19.3 cm/ka.

Figure 12. Tectonic model to explain the rotated ChRM declination record of the Cava Danesi Loess section. In (a) aerial view of the outcrop area and geological profiles along wall exposures showing the loess and fluvial/alluvial sediments affected by faulting as described in detail in Livio et al. (2014, 2020). In (b) modelling of Phase 1 of the deformation history of the Cava Danesi Loess section. The ChRM declination record from Figure 3c is transformed from depth to time according to the age model of Figure 10 and translated in order to attain 0° mean declination at either t = 11ka (end of observed record; yellow line) or t = 0 (red line). This implies 0.43°±2.5°/ka of syn-depositional clockwise rotation of the sequence ending anytime between 11 ka and modern times (gray area with question mark). The block diagram in (b) shows the fault kinematics considered responsible for the observed rotation. In (c) modeling of Phase 2 of the deformation history of the Cava Danesi Loess section. Sometimes after 11 ka, the ChRM declination record experienced a rigid-body counterclockwise rotation of 15-19° to attain the present-day geometry (green line, same as in Fig. 2c). Depicted is also a block diagram showing the fault kinematics during Phase 2. See text for discussion.

Supplementary Information

Figure S1. Google Earth image (upper panel) and photograph (lower panel) of the loess sequence and underlying fluvial sediments at Cava Danesi located at the top of Monte Netto hillock, with geometric, structural, and stratigraphic relationships of the loess sequence (units PL1-PL4) and underlying fluvial sediments (unit PL5). The positions of the Cava Danesi Loess section (units PL1-PL4) and the Cava Danesi Fluvial section (unit PL5) relative to the fault-propagation fold are indicated.

Figure S2. The characteristic remanent magnetization (ChRM) component directions from the Cava Danesi Loess section were corrected for the tectonic trend (red lines in Fig. 3c, d) to obtain detrended (a) Declination and (b) Inclination values. The detrended inclinations were also corrected for sedimentary inclination shallowing with the E/I method (Tauxe and Kent, 2004) that yielded a flattening factor f = 0.86 (c) (see also Fig. S3).

Figure S3. Results of the E/I method of Tauxe and Kent (2004) to correct for inclination shallowing the detrended Cava Danesi Loess section record. Panel (a) is a plot of the elongation (E) *versus* inclination (I) as a function of flattening factor (f). The green line is the E/I trend from the TK03.GAD field model. Optimal correction is obtained with f = 0.86. Panel (b) is the cumulative distribution of the corrected inclinations with mean value (green vertical line) and 95% confidence limit (blue vertical lines). Calculated with PmagPy (Tauxe et al., 2016).

Table S1. Thermal demagnetization data of samples from Monte Netto.

Table S2. ChRM component analysis on samples from Monte Netto.

Table S3. VGP data and formulas used to calculate the parameters of VGP scatter (S’) and within site scatter (S_f) (Tauxe and Kent, 2004; McElhinny and McFadden, 1997).

Table S4. Input and output data used to calculate the age model of Figure 10.

Figure1

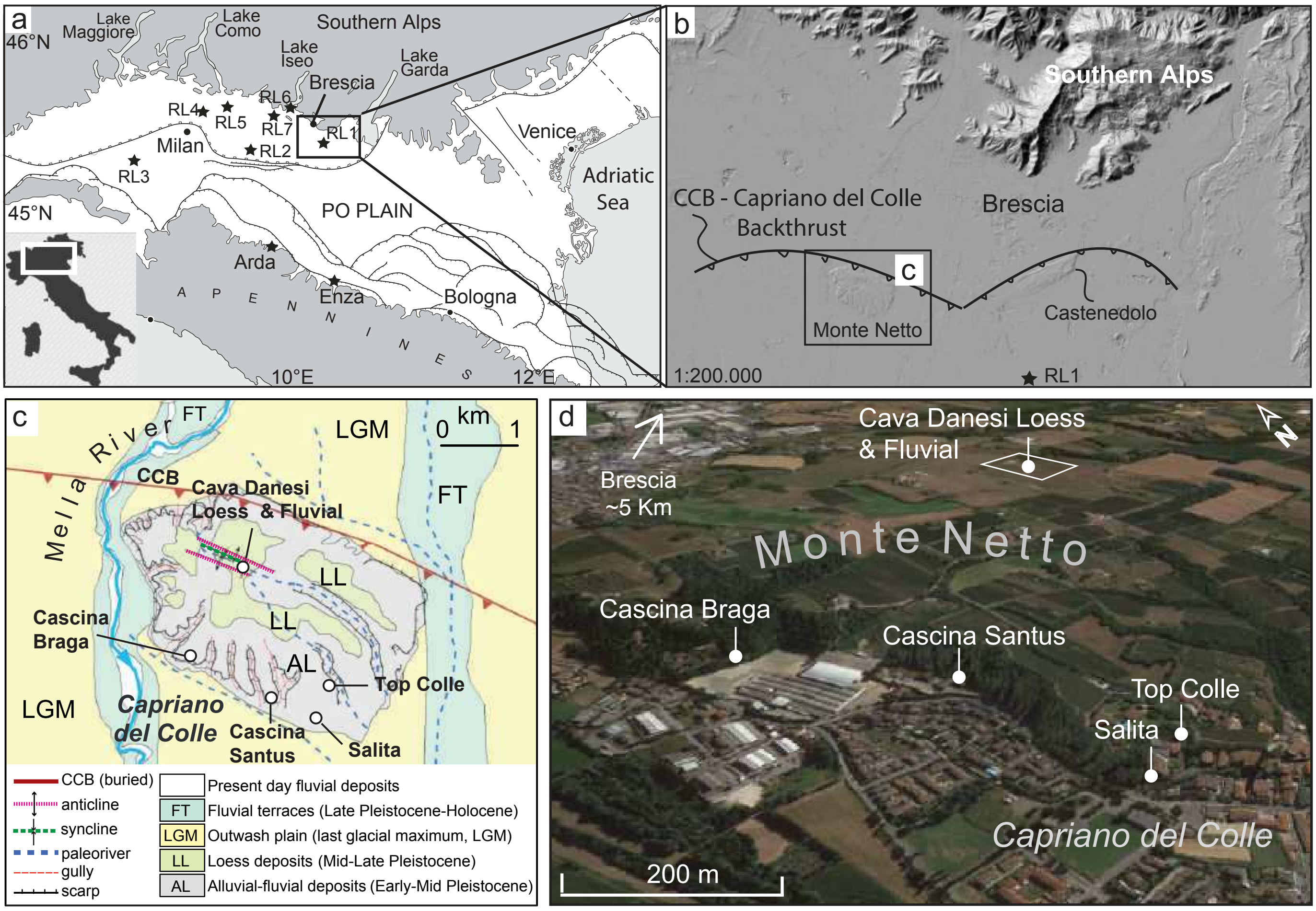
a
Lake Maggiore
Lake Como
Southern Alps
46°N
Lake Iseo
Lake Garda
Brescia
RL4
RL5
RL6
RL7
RL1
Milan
RL2
RL3
Venice
Adriatic Sea
45°N
PO PLAIN
Arda
Enza
Bologna
A P E N N I N E S
10°E
12°E
b
Southern Alps
CCB - Capriano del Colle Backthrust
Brescia
c
Monte Netto
Castenedolo
1:200.000
RL1
c
FT
LGM
0 km 1
Mella River
CCB
Cava Danesi Loess & Fluvial
FT
LL
LL
Cascina Braga
AL
Top Colle
LGM
Capriano del Colle
Cascina Santus
Salita
CCB (buried)
anticline
syncline
paleoriver
gully
scarp
Present day fluvial deposits
FT Fluvial terraces (Late Pleistocene-Holocene)
LGM Outwash plain (last glacial maximum, LGM)
LL Loess deposits (Mid-Late Pleistocene)
AL Alluvial-fluvial deposits (Early-Mid Pleistocene)
d
Brescia ~5 Km
Cava Danesi Loess & Fluvial
N
Monte Netto
Cascina Braga
Cascina Santus
Top Colle
Salita
Capriano del Colle
200 m

Figure2

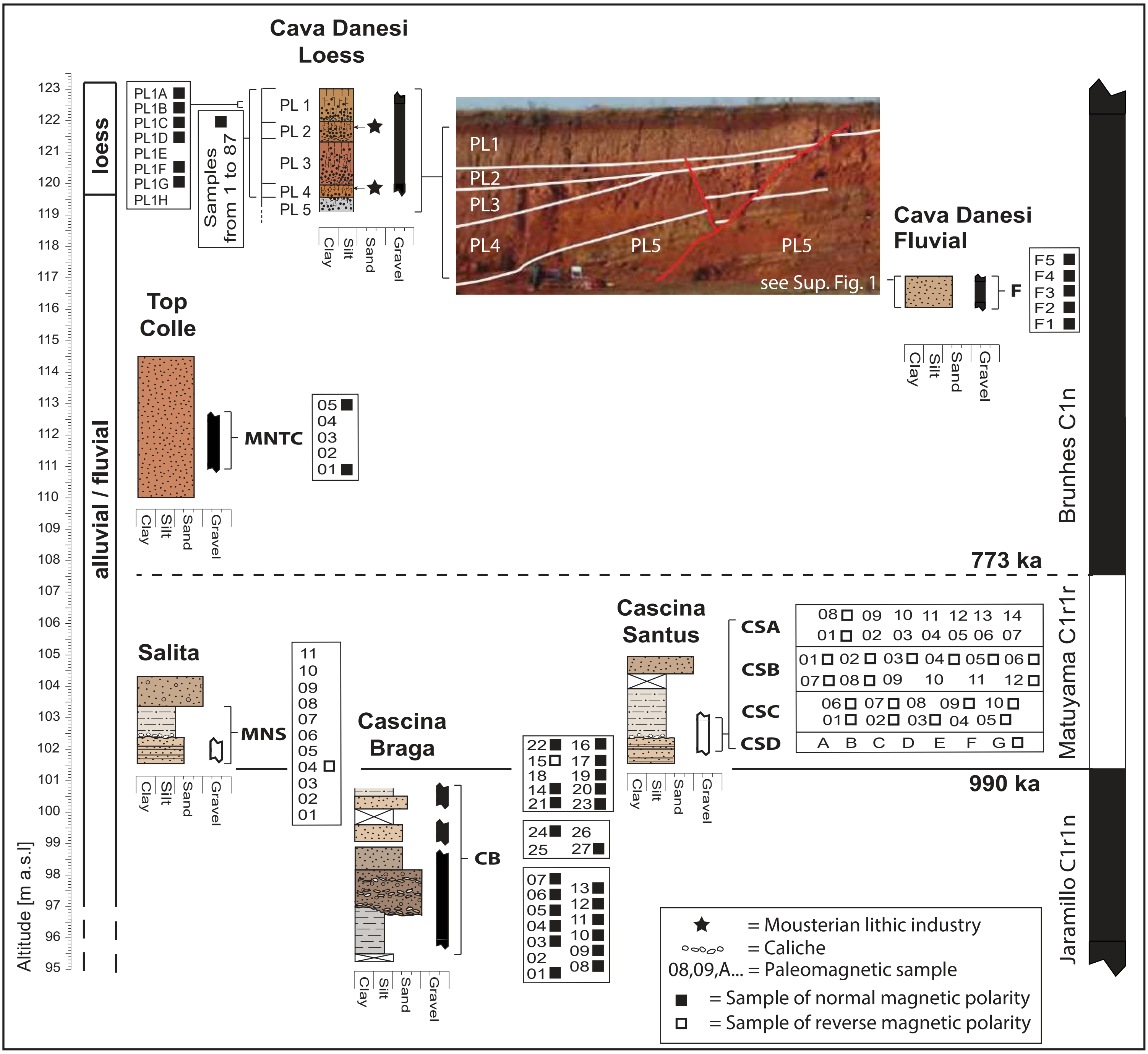
Cava Danesi Loess
Altitude [m a.s.l]
loess
alluvial / fluvial
PL1A PL1B PL1C PL1D PL1E PL1F PL1G PL1H
Samples from 1 to 87
PL 1 PL 2 PL 3 PL 4 PL 5
Clay Silt Sand Gravel
PL1 PL2 PL3 PL4 PL5 PL5
see Sup. Fig. 1
Cava Danesi Fluvial
F
F5 F4 F3 F2 F1
Top Colle
MNTC
05 04 03 02 01
773 ka
Brunhes C1n
Matuyama C1r1r
Jaramillo C1r1n
990 ka
Salita
MNS
11 10 09 08 07 06 05 04 03 02 01
Cascina Braga
CB
22 16 15 17 18 19 14 20 21 23
24 26 25 27
07 06 05 04 03 02 01 13 12 11 10 09 08
Cascina Santus
CSA CSB CSC CSD
08 09 10 11 12 13 14
01 02 03 04 05 06 07
01 02 03 04 05 06
07 08 09 10 11 12
06 07 08 09 10
01 02 03 04 05
A B C D E F G
= Mousterian lithic industry
= Caliche
08,09,A... = Paleomagnetic sample
= Sample of normal magnetic polarity
= Sample of reverse magnetic polarity

Figure3

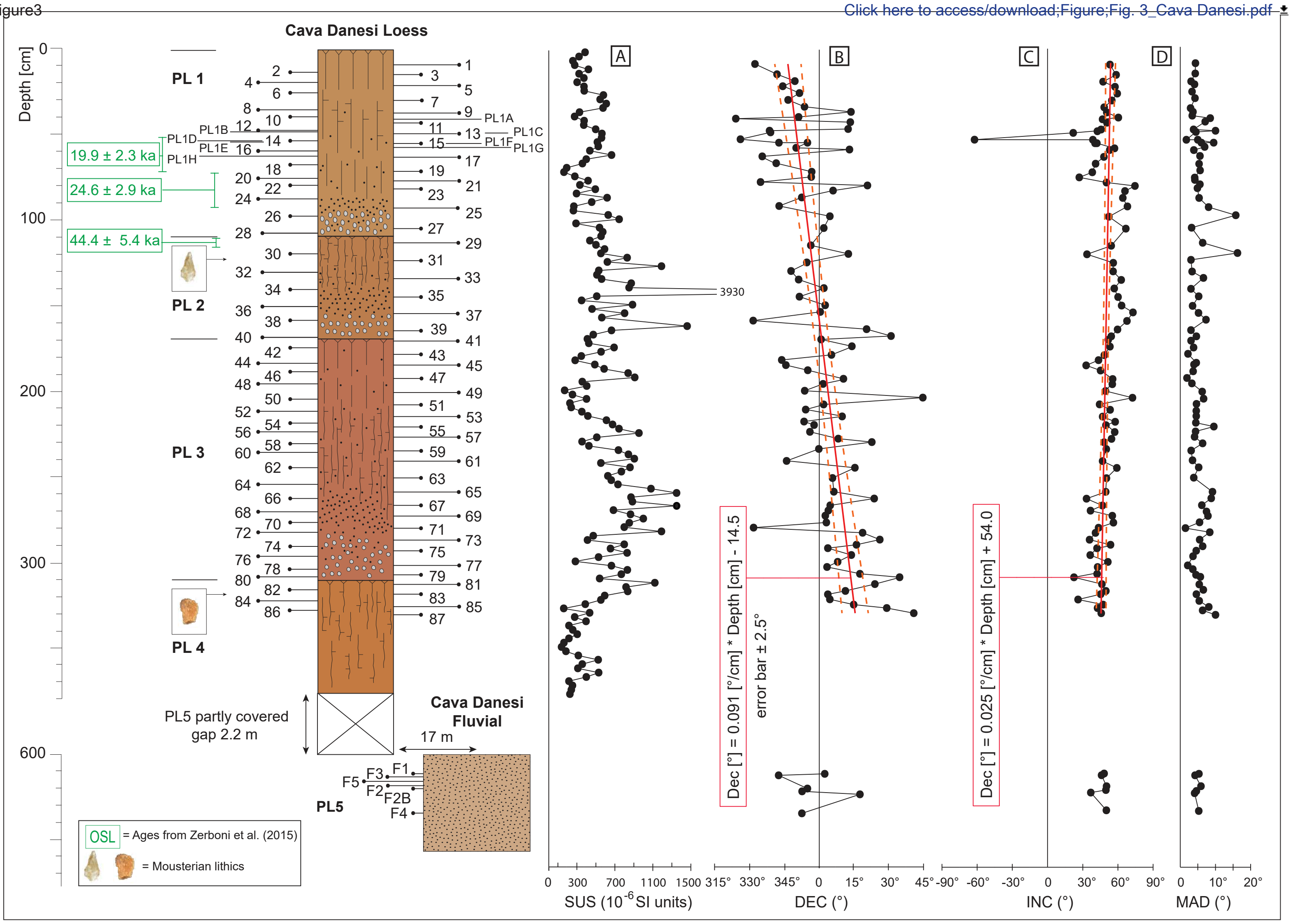
Cava Danesi Loess
Depth [cm]
PL 1
PL 2
PL 3
PL 4
19.9 ± 2.3 ka
24.6 ± 2.9 ka
44.4 ± 5.4 ka
PL5 partly covered gap 2.2 m
Cava Danesi Fluvial
17 m
PL5
OSL = Ages from Zerboni et al. (2015)
= Mousterian lithics
3930
Dec [°] = 0.091 [°/cm] * Depth [cm] - 14.5
error bar ± 2.5°
Dec [°] = 0.025 [°/cm] * Depth [cm] + 54.0
SUS (10^-6 SI units)
DEC (°)
INC (°)
MAD (°)
A
B
C
D

Figure4

Click here to access/download;Figure;Fig. 4_Rock Mag_Lowrie+IRM.pdf

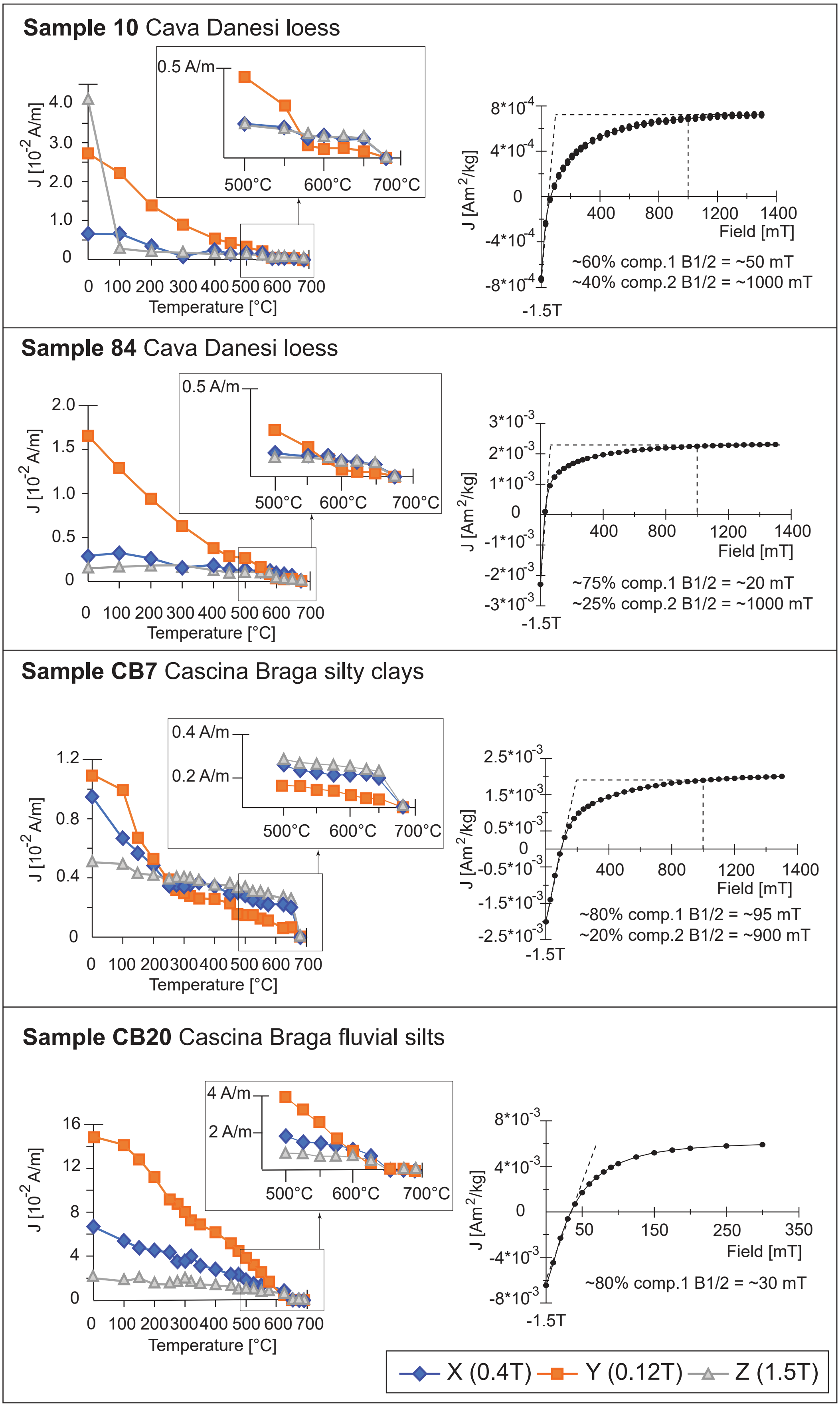

Figure5

Click here to access/download;Figure;Fig. 5_Rock Mag_Forc+Hys.pdf

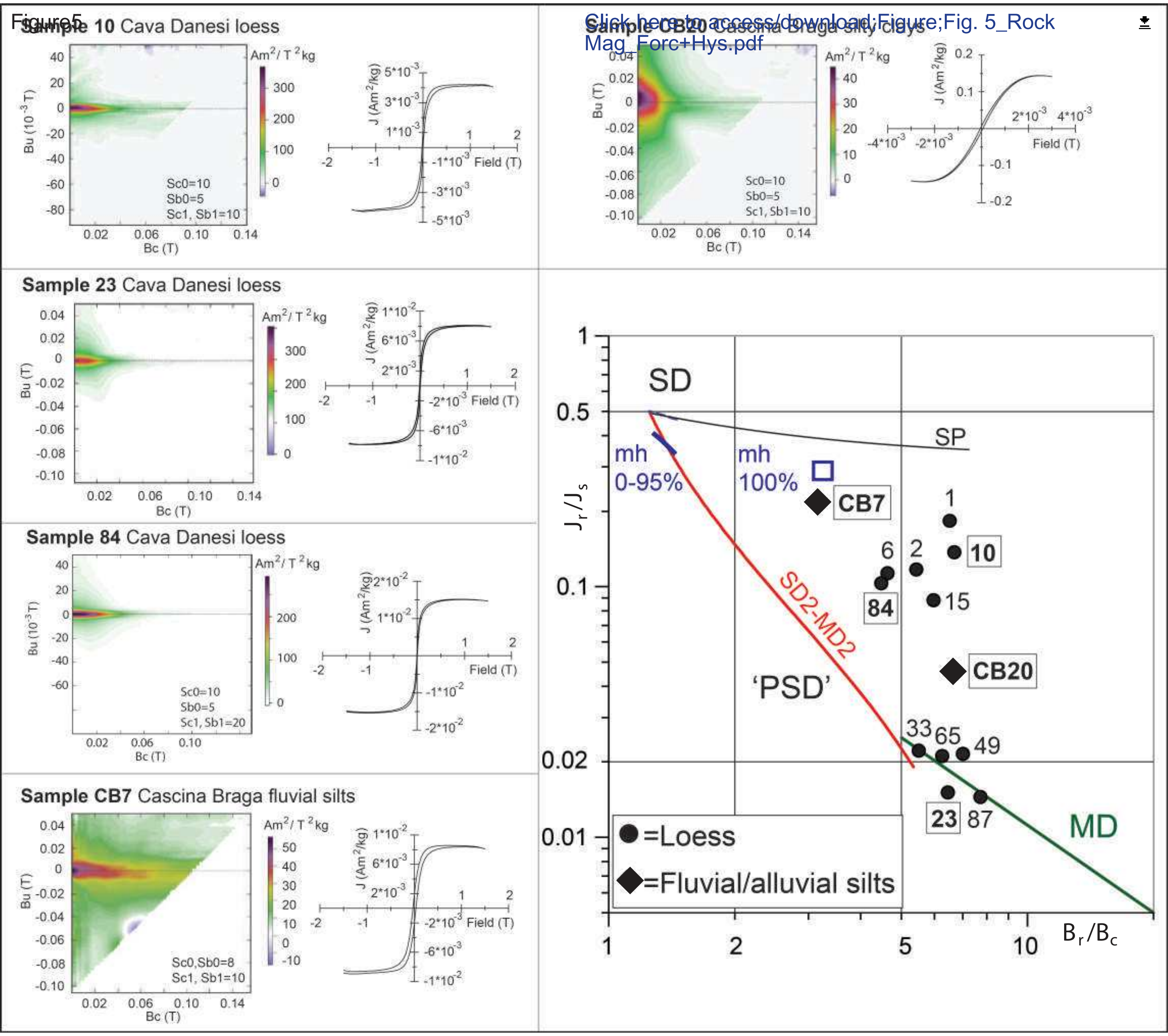

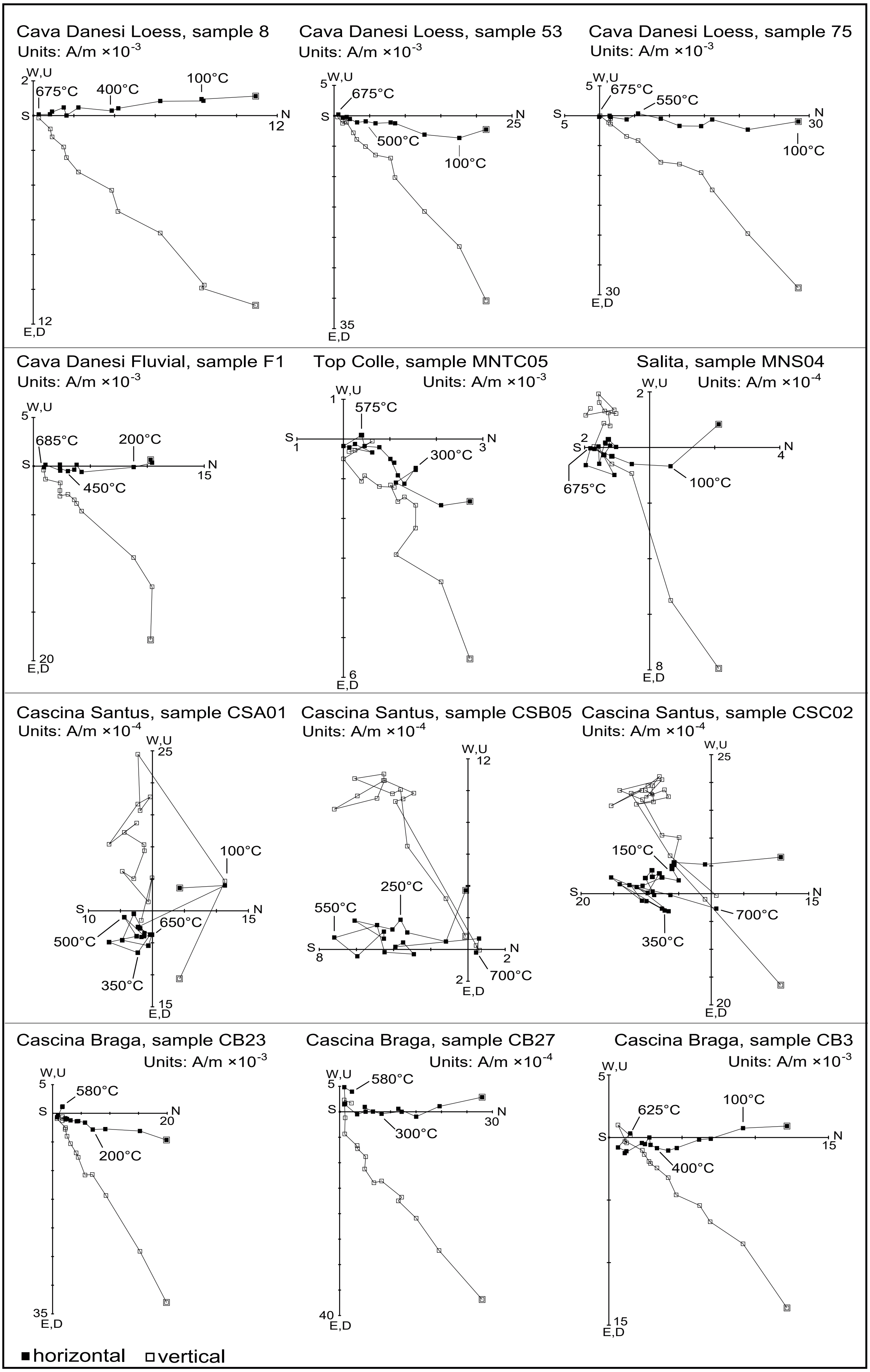
Cava Danesi Loess, sample 8
Units: A/m ×10^-3
675°C
400°C
100°C
Cava Danesi Loess, sample 53
Units: A/m ×10^-3
675°C
500°C
100°C
Cava Danesi Loess, sample 75
Units: A/m ×10^-3
675°C
550°C
100°C
Cava Danesi Fluvial, sample F1
Units: A/m ×10^-3
685°C
200°C
450°C
Top Colle, sample MNTC05
Units: A/m ×10^-3
575°C
300°C
Salita, sample MNS04
Units: A/m ×10^-4
675°C
100°C
Cascina Santus, sample CSA01
Units: A/m ×10^-4
100°C
650°C
500°C
350°C
Cascina Santus, sample CSB05
Units: A/m ×10^-4
250°C
550°C
700°C
Cascina Santus, sample CSC02
Units: A/m ×10^-4
150°C
700°C
350°C
Cascina Braga, sample CB23
Units: A/m ×10^-3
580°C
200°C
Cascina Braga, sample CB27
Units: A/m ×10^-4
580°C
300°C
Cascina Braga, sample CB3
Units: A/m ×10^-3
100°C
625°C
400°C
W,U
E,D
S
N
■horizontal □vertical

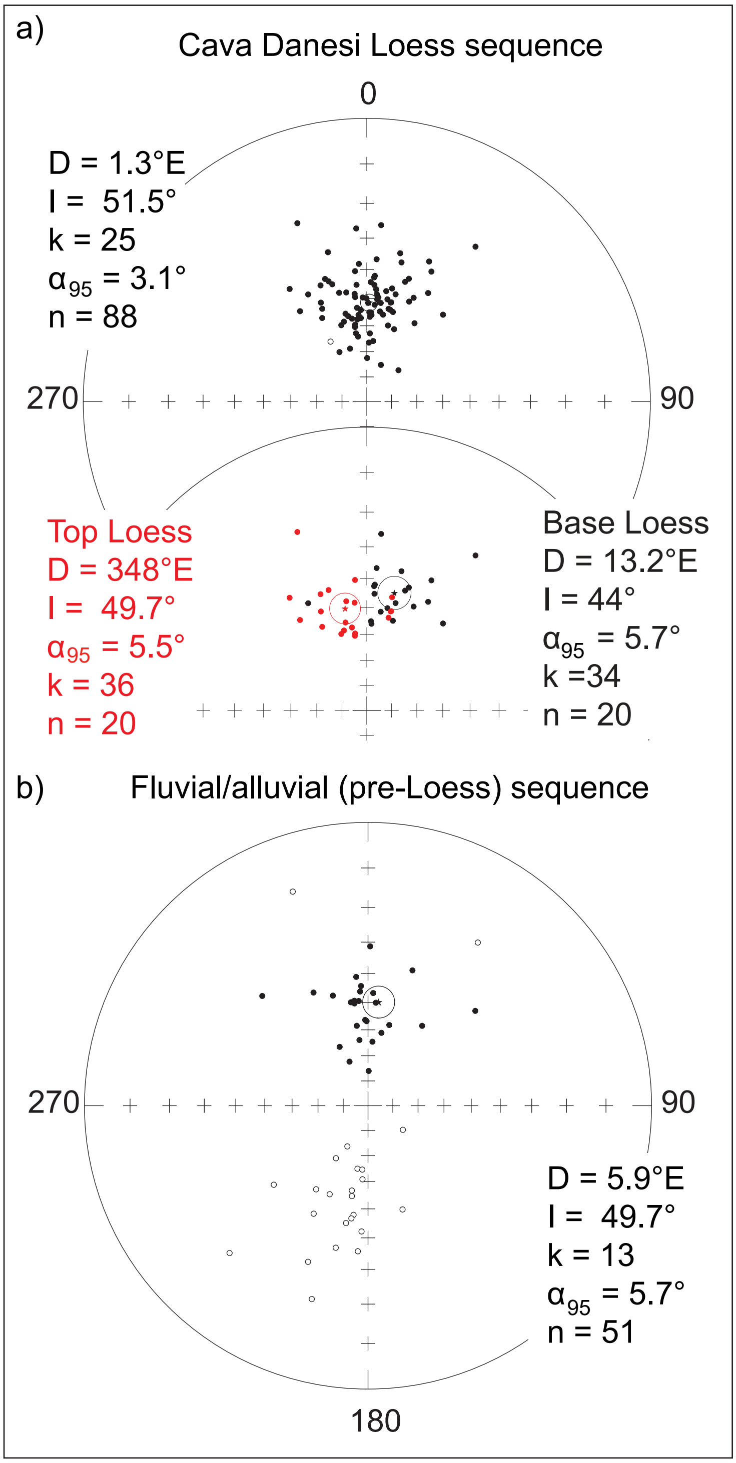
a)
Cava Danesi Loess sequence
0
D = 1.3°E
I = 51.5°
k = 25
α95 = 3.1°
n = 88
270
90
Top Loess
D = 348°E
I = 49.7°
α95 = 5.5°
k = 36
n = 20
Base Loess
D = 13.2°E
I = 44°
α95 = 5.7°
k =34
n = 20
b)
Fluvial/alluvial (pre-Loess) sequence
270
90
D = 5.9°E
I = 49.7°
k = 13
α95 = 5.7°
n = 51
180

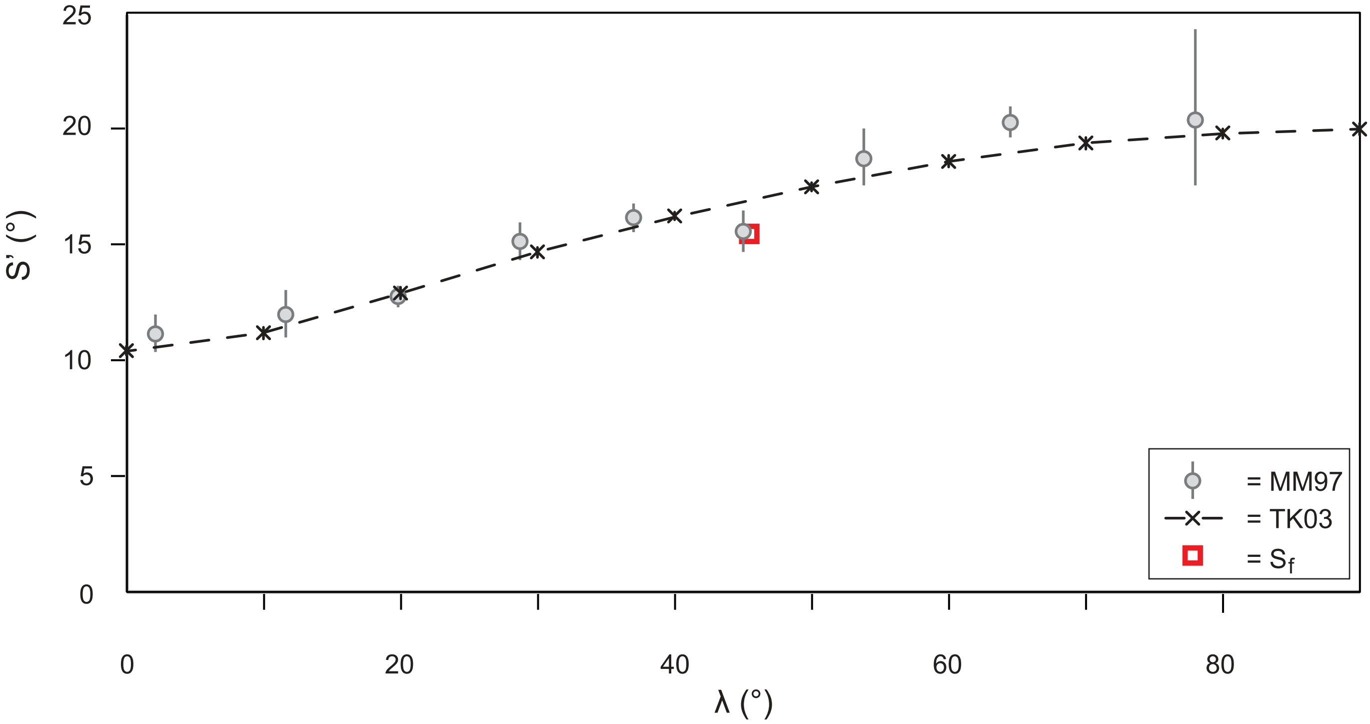
25
20
15
10
5
0
S' (°)
0
20
40
60
80
λ (°)
= MM97
= TK03
= S_f

Figure9

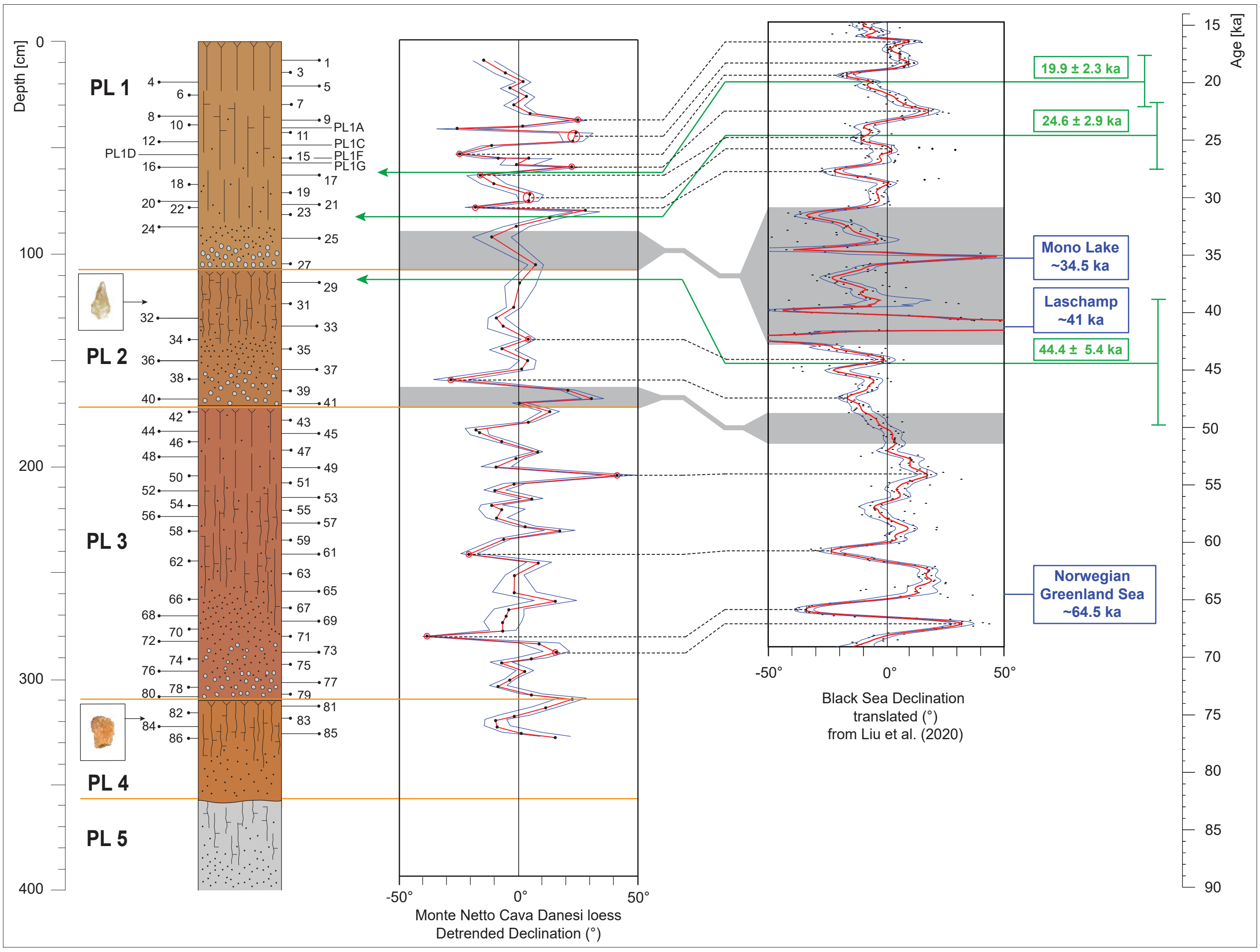

Depth [cm]
0
100
200
300
400
PL 1
PL 2
PL 3
PL 4
PL 5
PL1A
PL1C
PL1D
PL1F
PL1G
-50°
0°
50°
Monte Netto Cava Danesi loess
Detrended Declination (°)
Black Sea Declination
translated (°)
from Liu et al. (2020)
19.9 ± 2.3 ka
24.6 ± 2.9 ka
44.4 ± 5.4 ka
Mono Lake
~34.5 ka
Laschamp
~41 ka
Norwegian
Greenland Sea
~64.5 ka
Age [ka]
15
20
25
30
35
40
45
50
55
60
65
70
75
80
85
90

Figure 10

Click here to access/download;Figure;Fig. 10_PSV age model.pdf

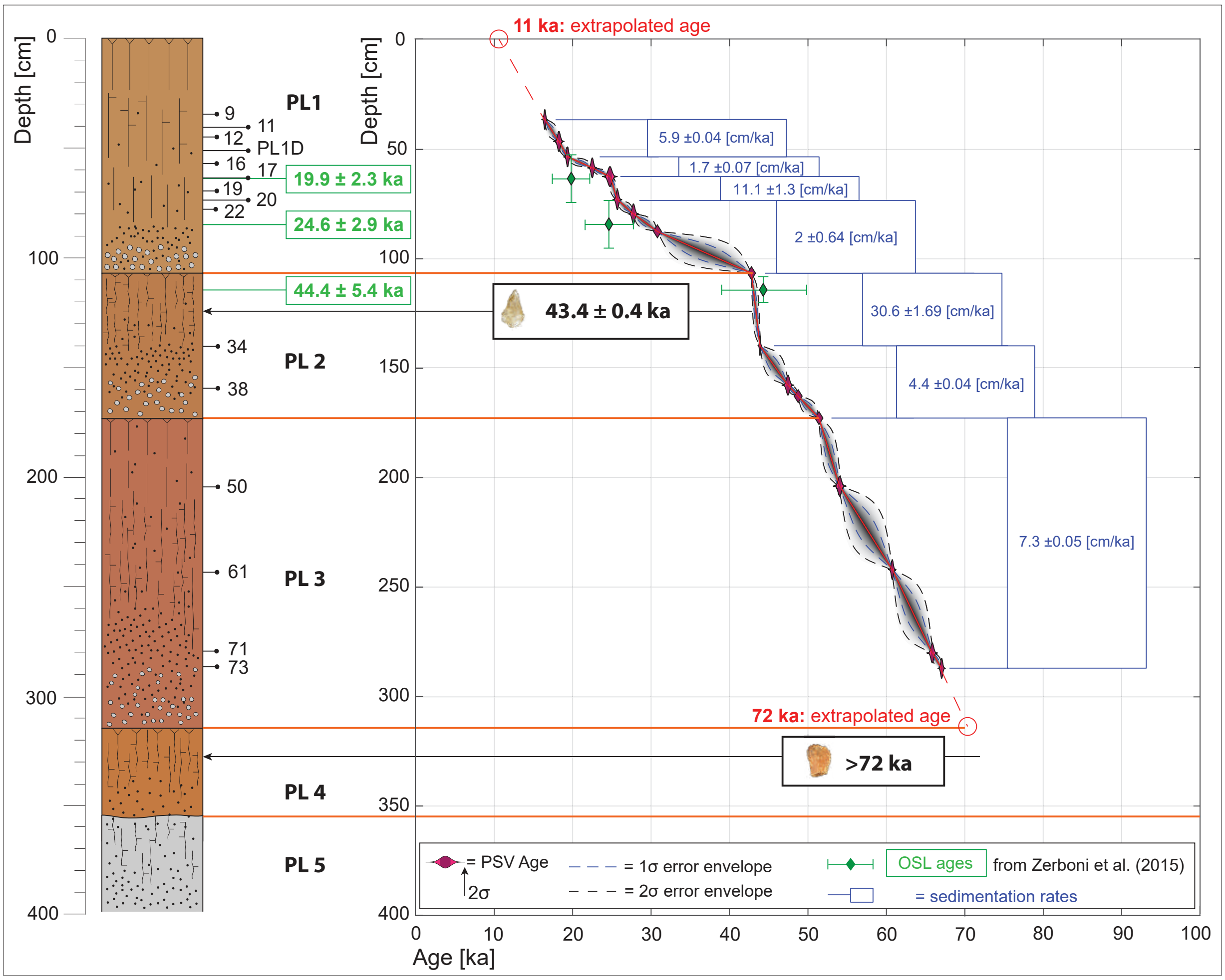

Figure11

Click here to access/download;Figure;Fig.11_uplift.pdf

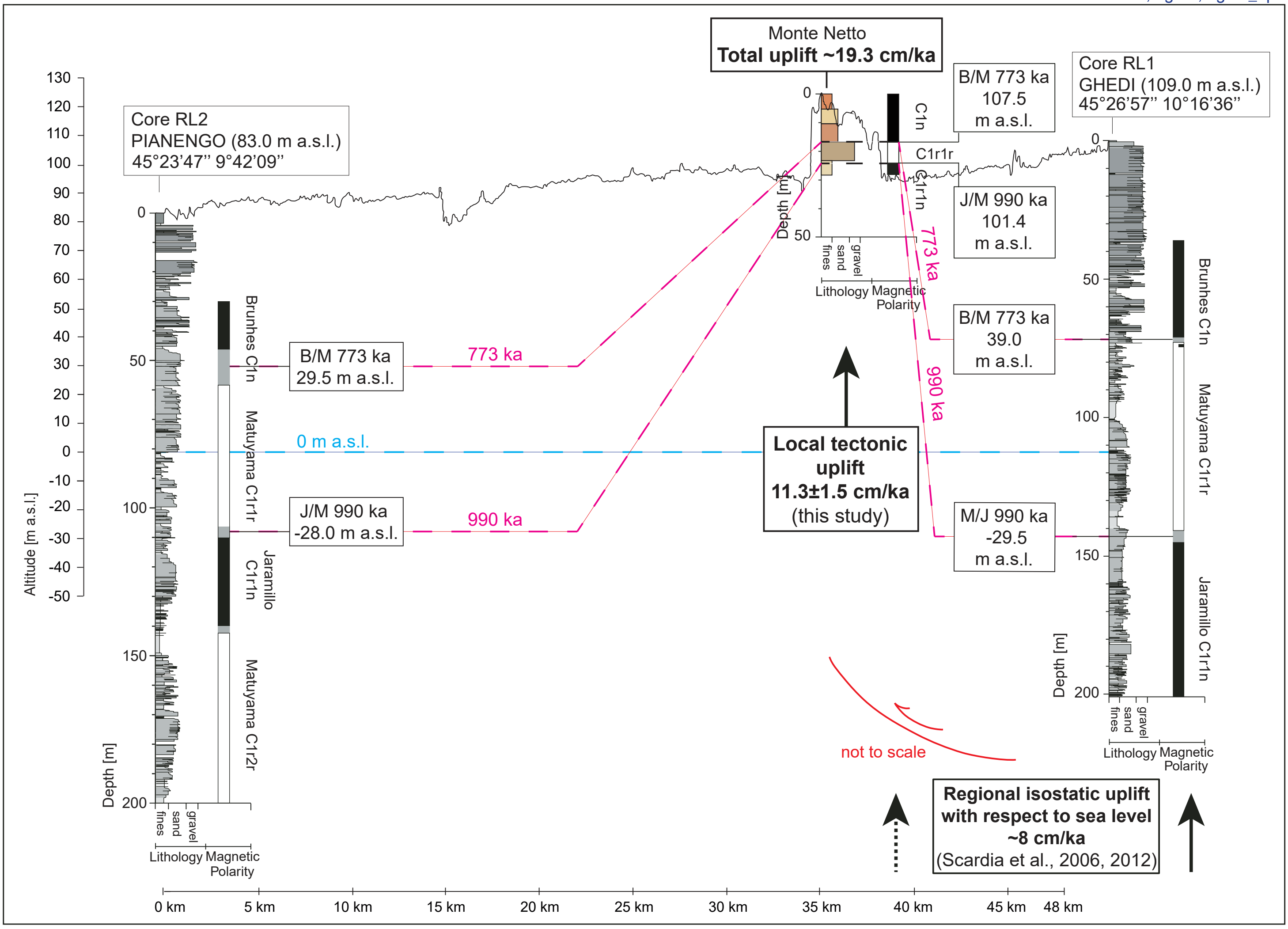

Figure12

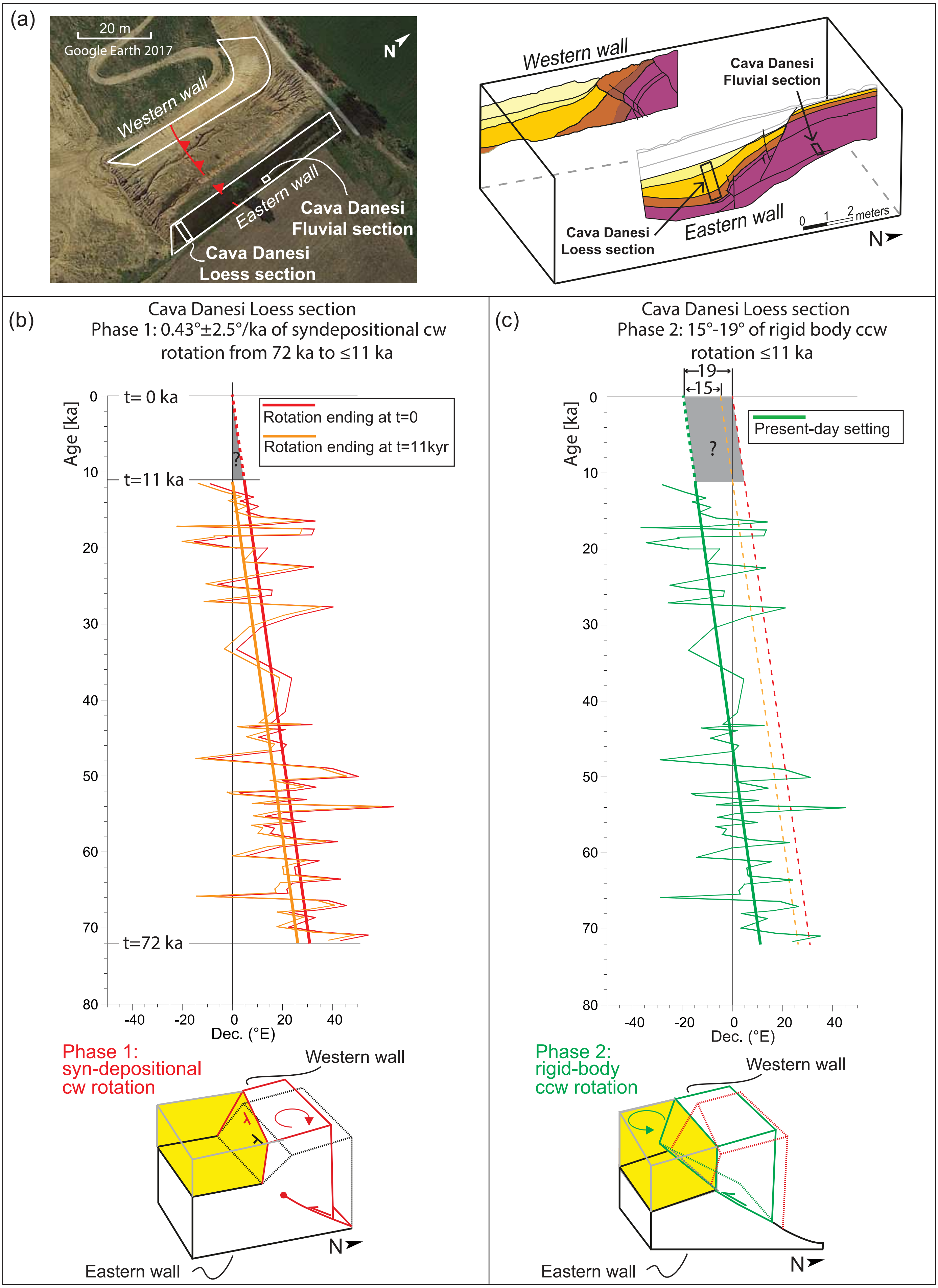
(a)
20 m
Google Earth 2017
N
Western wall
Eastern wall
Cava Danesi Fluvial section
Cava Danesi Loess section
Western wall
Cava Danesi Fluvial section
Cava Danesi Loess section
Eastern wall
0 1 2 meters
N
(b)
Cava Danesi Loess section
Phase 1: 0.43°±2.5°/ka of syndepositional cw rotation from 72 ka to ≤11 ka
Age [ka]
t= 0 ka
t=11 ka
t=72 ka
Rotation ending at t=0
Rotation ending at t=11kyr
Dec. (°E)
Phase 1: syn-depositional cw rotation
Western wall
Eastern wall
N
(c)
Cava Danesi Loess section
Phase 2: 15°-19° of rigid body ccw rotation ≤11 ka
19
15
Present-day setting
Age [ka]
Dec. (°E)
Phase 2: rigid-body ccw rotation
Western wall
Eastern wall
N